nature biomedical engineering

Article

https://doi.org/10.1038/s41551-024-01280-w

A stealthy neural recorder for the study of behaviour in primates

Received: 5 July 2023

Accepted: 8 October 2024

Published online: 8 November 2024

Check for updates

Saehyuck Oh[1,2,19], Janghwan Jekal[1,2,19], Jinyoung Won[3,19], Kyung Seob Lim[4], Chang-Yeop Jeon[3], Junghyung Park[3], Hyeon-Gu Yeo[3,5], Yu Gyeong Kim[3,5], Young Hee Lee[6,7], Leslie Jaesun Ha[6,7], Han Hee Jung[1,2], Junwoo Yea[1,2], Hyeokjun Lee[1,2], Jeongdae Ha[1,2], Jinmo Kim[2,8], Doyoung Lee[2,8], Soojeong Song[1,2], Jieun Son[1,2], Tae Sang Yu[1,2], Jungmin Lee[9], Sanghoon Lee[1], Jaehong Lee[1], Bong Hoon Kim[1], Ji-Woong Choi[2,8], Jong-Cheol Rah[10,11], Young Min Song[12], Jae-Woong Jeong[13], Hyung Jin Choi[6,7], Sheng Xu[14], Youngjeon Lee[3,5] ✉ & Kyung-In Jang[1,2,8,10,11,15,16,17,18] ✉

By monitoring brain neural signals, neural recorders allow for the study of neurological mechanisms underlying specific behavioural and cognitive states. However, the large brain volumes of non-human primates and their extensive range of uncontrolled movements and inherent wildness make it difficult to carry out covert and long-term recording and analysis of deep-brain neural signals. Here we report the development and performance of a stealthy neural recorder for the study of naturalistic behaviours in non-human primates. The neural recorder includes a fully implantable wireless and battery-free module for the recording of local field potentials and accelerometry data in real time, a flexible 32-electrode neural probe with a resorbable insertion shuttle, and a repeater coil-based wireless-power-transfer system operating at the body scale. We used the device to record neurobehavioural data for over 1 month in a freely moving monkey and leveraged the recorded data to train an artificial intelligence model for the classification of the animals' eating behaviours.

The brain is the central organ of the body that orchestrates physical and mental activities ranging from trivial movements to highly functional cognitive behaviour. In modern society, destructive incurable diseases that affect a large number of patients around the world, such as Alzheimer's disease, Parkinson's disease, epilepsy, depression and addiction, originate from neurological deterioration of the complex brain neural network. Therefore, recent advancements in biomedical engineering have led to the identification and management of the relationship between brain neural activity and certain psycho-physical states or behaviours, which has helped elucidate the cause of neurodegenerative brain diseases and has paved the way for early diagnosis and accurate treatment[1–6].

In conventional brain neural interface technology, a rigid silicon-based neural probe embedded in the brain collects neural signals under physically restrained or anaesthetized conditions, and a head-mounted device powered by batteries subsequently amplifies, filters and digitizes those signals. Then, wired external equipment extracts features of biological information from brain neural activity through further signal analysis[7–9]. With recent advances in bioelectronics, flexible neural probes fabricated by utilizing biocompatible materials and semiconductor technologies achieve chronic neural signal recording with a minimally invasive approach[10–13]. Furthermore, wireless power transfer and wireless communication enable the design of fully implantable neural interface devices, allowing animals to behave naturally in an untethered environment by removing hazardous batteries and external electrical wires[14–18].

Non-human primates (NHPs) exhibit phylogenetic proximity and close similarities to humans, including the ability to perform complex

A full list of affiliations appears at the end of the paper. ✉e-mail: neurosci@kribb.re.kr; kijang@dgist.ac.kr

brain neuronal functions that result in highly functional cognitive and social behaviours. They also provide important translational clinical insights before implementing brain implants on humans in biomedical neuroscience research[19,20]. However, most brain neuro-engineering studies have been limited to small-animal models such as rodents. It is highly challenging to develop a single integrated neural interface system that can record real-time brain neural signals, store data on a server, analyse signals and combine different device functions, including multimodal signal measurement, wireless power harvesting, wireless communication and device control, into a single implantable device in NHPs for the study of brain neuronal dynamics of natural instincts. First, the brain volume of NHPs is more than 50 times larger than that of rodents. Due to the large size of the brain, it is difficult to insert a long neural probe with low bending stiffness by mimicking the brain's compliance (a few kPa). Second, NHPs sit, stand and hang in a flexible posture with their four limbs. This NHPs' freedom of movement, which allows them to adjust the height and angle of their heads, presents a major challenge in providing stable wireless power. For these reasons, there have been few studies on brain neural interface technology in NHPs[21–23]. While neural probes have greatly advanced our understanding of cortical functions in cognition, they also present challenges in fully exploring the complex interplay between deep brain structures, cortical areas and behavioural outcomes. In addition, most neural interface devices often use a potentially hazardous rechargeable battery or short-range wireless power transfer, which requires the monkey to move or be restrained to a charging station. This limitation makes it difficult to seamlessly record neural activity for studying naturalistic behaviours. Overall, due to the aforementioned large-animal-specific technical challenges, there is no neatly integrated wireless, battery-free, fully implantable neural interface for monitoring the brain neural activity of NHPs' natural instinctive behaviour in an unrestricted, wild-like environment (Extended Data Fig. 1a and Supplementary Table 1).

Here we introduce a class of stealthy neural recorders in untethered, conscious and freely moving NHPs, covering (1) a wireless, battery-free, fully implantable embedded system device with real-time neurobehavioural signal recording (multichannel neural signal and acceleration signal corresponding to NHPs' instinctive behaviours) in a user-friendly smartphone interface; (2) a flexible 32-electrode neural probe coated with a bioresorbable, mechanically transient sucrose insertion shuttle; (3) submetre-scale wireless power transfer by a precisely coupled repeater-coil system; and (4) artificial intelligence (AI) modelling for brain neurobehavioural analysis to classify the natural instinctive behaviours of NHPs.

Results

Overview of neurobehavioural research using the stealthy neural recorder

The stealthy neural recorder is a wireless, battery-free and low-power (average, ~25 mW, Supplementary Fig. 11) brain neural implant that is conformably implanted under the scalp of awake, freely moving NHPs to measure neural signals from deep brain regions and to extract behavioural features for neurobehavioural analysis during unconstrained instinctive behaviours (such as eating) (Fig. 1 and Extended Data Fig. 1b). A customized smartphone application monitors the neurobehavioural signals from the brain and synchronizes them to the server to accumulate biophysiological big data (Extended Data Fig. 2 and Supplementary Video 1). Collected large-capacity brain neural signals are converted into scalograms for time-frequency representations, and acceleration signals (ACC) are processed to extract average intensity and standard deviation. Then, the processed signals are used as distinguishable features to uncover digital biomarkers inherent in the signals. The developed AI model constructs an artificial neural network with extracted digital biomarkers and then learns to classify and determine the neurobehavioural states of NHPs exhibiting instinctive behaviours. AI model-based neurobehavioural analysis provides a scientific basis for identifying a psycho-physical correlation between neural activity at the specific brain region and corresponding behaviours to rationalize unidentified hypotheses in brain neuroscience research. This technology can extract and analyse neurophysiological data collected directly from the brain to provide integrative, scientific and objective brain neurobehavioural knowledge by correlating physical behaviours captured by the traditional camera-based system and neurological data recorded by the proposed neural recorder.

The neural recorder consists of a long (~7.7 cm) flexible neural probe with 32 electrodes to collect neural signals in the deep brain region and a main embedded circuit with functional layers for signal measurement, wireless power harvesting and wireless communication units (Fig. 2a,b and Extended Data Fig. 3a). Figure 2a illustrates schematics of the proposed flexible neural probe. The double layer of patterned metal (Cr/Au, 7/200 nm) provides a seed layer for three-dimensional (3D) nanoporous microelectrodes (Pt/IrOx), captures raw neural signals and transmits them to the neural recorder. Thin layers of polyimide (PI, 1-3 μm) films insulate adjacent metal layers and serve as an encapsulant to prevent electrical leakage. The porous structure with a size of hundreds of nanometres (~220 nm) minimizes the electrochemical impedance (~37 kΩ) of electrodes to maximize the signal-to-noise ratio of the neural signal. The U-beam-shaped bioresorbable, mechanically transient insertion shuttle provides reliable insertion of the flexible neural probe without buckling.

Figure 2b presents the heterogeneous architecture of the stealthy neural recorder with thin functional layers that eliminate the need for batteries and external electrical wires, allowing the recorder to be completely implanted under the scalp in a biocompatible form (Extended Data Fig. 3b). The neural recorder (radius = 30 mm and height = 3 mm) consists of the uppermost wireless power receiver to harvest power from the generated surrounding magnetic field and the bottom embedded system to measure neurobehavioural signals and transmit the dataset by wireless communication. In detail, a litz coil with a centre frequency of 13.56 MHz receives the wireless power to operate the embedded system, while the flexible ferrite sheet (0.1 mm thickness) guides the magnetic flux to maximize wireless power transfer efficiency. Next, ground planes (17.5 μm thickness) serve as a sink for return currents circulating through the board to minimize electromagnetic interference (EMI) noise and provide radio frequency (RF) radiation for reliable wireless communication. The robust RF radiation in the ground plane allows the device to maintain a high data rate (>60 kBps) up to 7 m from the smartphone, which is comparable to a battery-powered device, even under a strong magnetic field (Extended Data Fig. 3c). Moreover, a copper sheet (0.1 mm thickness) is attached underneath the circuit to protect it from magnetic flux near the coil. Lastly, chemical vapour-deposited Parylene-C film (18 μm thickness), serving as the outermost layer of the device, prevents critical penetration of biological fluids around the device, while low-modulus silicone serves as soft encapsulation. With this design, the stealthy neural recorder is fully integrated (Fig. 2c,d and Extended Data Fig. 4a) and implanted between the skull and scalp of the monkey (Fig. 2e and Extended Data Fig. 4b).

Flexible deep brain neural probe with a bioresorbable insertion shuttle

Flexible neural probes enable chronic neural recording with less damage to the brain[10–12], but their low mechanical stiffness makes them floppy and difficult to insert into the brain[24]. To insert a flexible neural probe into the deep brain region of NHPs, a strategy to impart temporary stiffness to the probe is needed. As an ideal candidate, sucrose is a biocompatible, bioresorbable, sufficiently rigid and thermally processible material[25]. Utilizing the characteristic rheological behaviour of sucrose, we designed a bioresorbable, mechanically transient insertion shuttle using a stamp printing process (Extended Data Fig. 5b) and attached it to the neural probe to allow the electrodes to be inserted into the targeted area of the brain (Supplementary Video 2). After the neural

https://doi.org/10.1038/s41551-024-01280-w

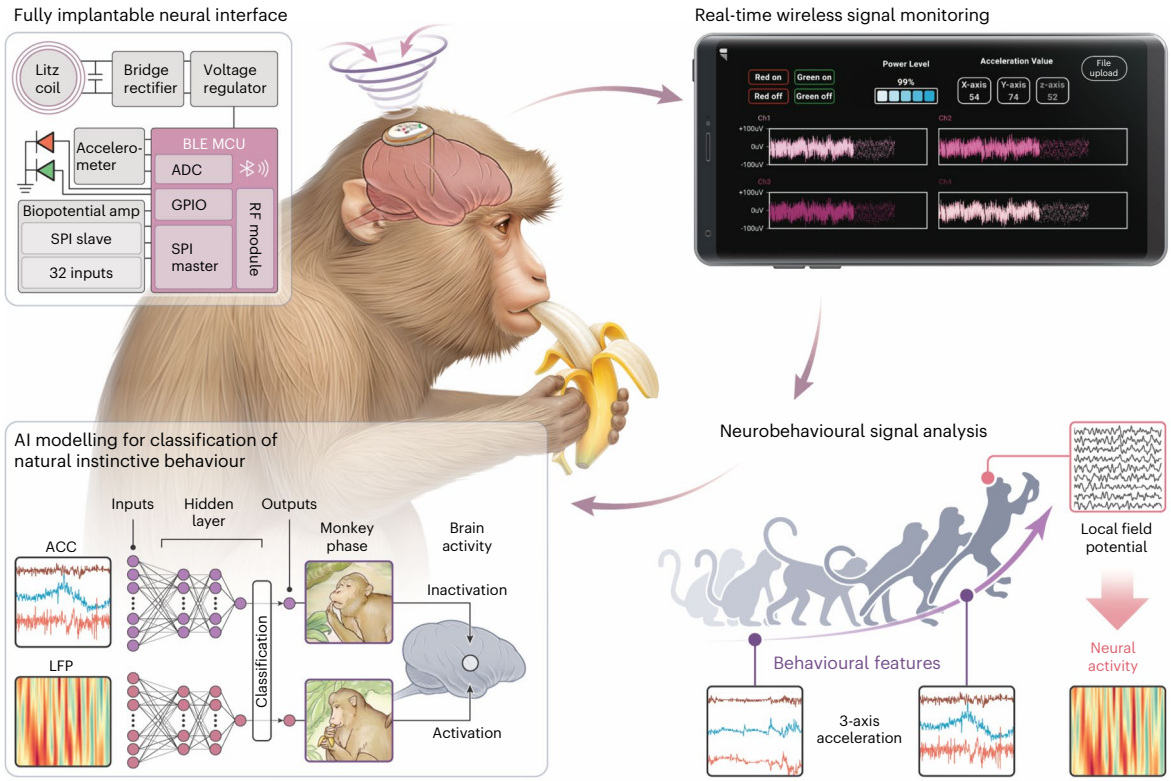

Fig. 1 | Neurobehavioural research of naturalistic behaviour in NHPs using a stealthy neural recorder. Conceptual flow diagram of neurobehavioural research using a stealthy neural recorder for studying naturalistic behaviour (such as eating) in untethered, conscious and freely moving NHPs. ADC, analogue-to-digital converter. GPIO, general purpose input–output. SPI, serial peripheral interface.

probe insertion step, the sucrose gradually dissolves and diffuses away into the surrounding biological fluids so that the electrodes are directly exposed to adjacent neurons to measure brain neural signals (Fig. 3a).

The optical image of the neural probe shows that the sucrose insertion shuttle dissolves away and leaves only a thin neural probe (~5 μm) to provide extremely high mechanical compliance and minimize brain damage (Fig. 3b(left)). Spatially mapped microelectrodes (8 × 4 matrix) enable multichannel neural recording in the target brain region (Fig. 3b(middle)). Each electrode has a 3D nanoporous structure composed of platinum (Pt) and a thin coating layer of iridium oxide (IrOx) fabricated by electrochemical deposition using polystyrene beads as a structural template (Extended Data Fig. 5a). Owing to their large effective area, the porous electrodes have a low electrochemical impedance (~37 kΩ), which allows them to measure electrophysiological signals reliably in the medium of the brain (Fig. 3b(right) and Supplementary Fig. 7). The fabrication strategy based on heterogeneous material design with structural modification of electrodes enables the construction of porous platinum-iridium oxide electrodes with ~40-times lower impedance than bare gold (Au) electrodes (Fig. 3f).

Through systematic mechanical design, we studied the theoretical moment of inertia as a function of the flange width and height of the U-beam-shaped sucrose insertion shuttle to define the criteria required to prevent undesired mechanical buckling of the neural probe during deep brain insertion in NHPs; we then set the design parameters (flange width/height = 100 μm/100 μm) to exceed the buckling threshold (Fig. 3c; see Supplementary Fig. 1 and Note 1 for details). The minimum force[26] to penetrate the white matter and insert a neural probe into the brain is known to be 1 mN. Conventional flexible neural probe designs with a long length for NHPs tend to have a low buckling force (0.006 mN), which leads to easy buckling and failure when attempting to penetrate the brain surface (Fig. 3d(left)). However, the proposed U-beam sucrose-coated neural probe design can be inserted into the brain without buckling due to its high buckling force threshold (90.578 mN) (Fig. 3d(right),g). An optical image of a partially dissolved sucrose-coated neural probe highlights the difference in mechanical stiffness between the parts with and without the sucrose insertion shuttle (Fig. 3e). Figure 3h comprehensively demonstrates the mechanically and electrochemically transient behaviour of the bioresorbable sucrose shuttle and the electrode during the insertion process of the proposed flexible neural probe. The sucrose insertion shuttle provides mechanical rigidity and a protective cover for the electrodes. After insertion, the sucrose dissolves and diffuses away within a few minutes (~5 min) to minimize brain damage. The subsequently exposed electrodes have a low electrochemical impedance (66 kΩ) to allow stable neural recording. Histological analysis of a rat and monkey brain demonstrates the minimal invasiveness of the proposed sucrose insertion shuttle by showing brain tissue recovery over time after neural probe insertion (Extended Data Fig. 6b,c). The serpentine interconnect of the neural probe differs in mechanical compliance from the injectable needle of the neural probe, providing strain relief and a mechanical buffer against elongation during device implantation to prevent the electrodes from moving out of their original insertion site when the device is positioned on the skull (Extended Data Figs. 4b and 5c).

A body-scale wireless power transfer for naturalistic behaviour

Wireless and battery-free bioelectronics operate by harvesting wireless power from the magnetic field generated by the wired external loop coil[15,16,18]. However, conventional wireless power transfer using a single transmitter coil cannot provide sufficient power to the implanted device in the head of a freely moving monkey within tens of centimetres of space to study instinctive behaviours in an unconstrained environment. To overcome this issue, the wireless power transfer range should

https://doi.org/10.1038/s41551-024-01280-w

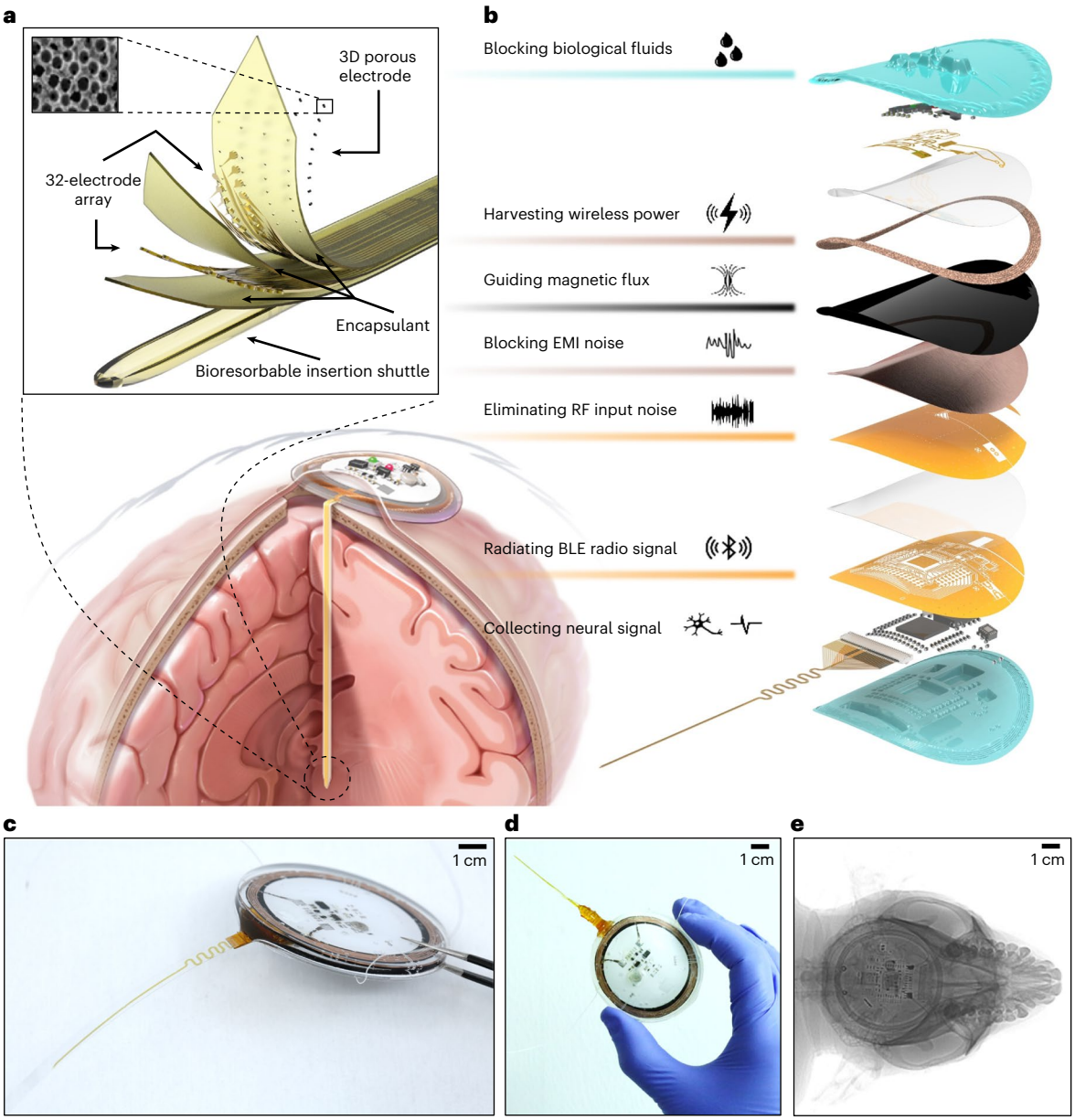

Fig. 2 | Design and configuration of a stealthy neural recorder for NHPs. **a**, Exploded view of a flexible neural probe with 3D nanoporous microelectrodes coated with a bioresorbable insertion shuttle for insertion into the deep brain area of NHPs. Inset: scanning electron microscope (SEM) image. **b**, Exploded view of the stealthy neural recorder with multifunctional layers. **c**,**d**, Optical images of the stealthy neural recorder. **e**, CT image of a cynomolgus monkey (*M. fascicularis*) head with the implanted stealthy neural recorder.

be extended by forwarding the magnetic field with the repeater coil[27] considering the loading effect and the coupling coefficient with the primary coil in a custom-designed wireless-power home cage (Fig. 4a). Therefore, the proposed repeater coil-based wireless power transfer system, termed the 'Repeater-Tx system', consists of a primary coil, repeater coil and receiver coil. This system is designed to concentrate a wide magnetic field in the target region around the monkey head to guarantee a wide wireless power transfer range for the freely moving monkey (Fig. 4b,c and Supplementary Video 3).

The conventional wireless power transfer system uses a single primary coil and a receiver coil as a pair, termed the 'Single-Tx system'. The primary coil of this system is wired to an external power supply that has inherent load resistance in the terminal, so the current flowing along the primary coil and the corresponding magnetic field is limited. As a result, the Single-Tx system suffers from a constrained operation range of the implanted device, causing the monkey to crouch in tight spaces (Fig. 4d). On the other hand, in the Repeater-Tx system, the current flowing along the repeater coil varies with the coupling coefficient according to the distance between the primary and the repeater coils (Fig. 4e). Through analytical circuit analysis and a careful tuning process, we derived a critically coupled range of the coupling coefficient in which the current flowing in the repeater coil of the Repeater-Tx system is larger than that in the primary coil of the Single-Tx system (Supplementary Notes 2 and 3 and Figs. 13 and 14). Then, the primary and repeater coils of the Repeater-Tx system were placed in that range to generate a wide magnetic field (Fig. 4f–i; see Supplementary Figs. 2 and 3 for details of the system configuration). With this configuration, the Repeater-Tx system was demonstrated to enable wireless connection and signal measurement in a large space to accommodate free NHP behaviour (Fig. 4j,k).

https://doi.org/10.1038/s41551-024-01280-w

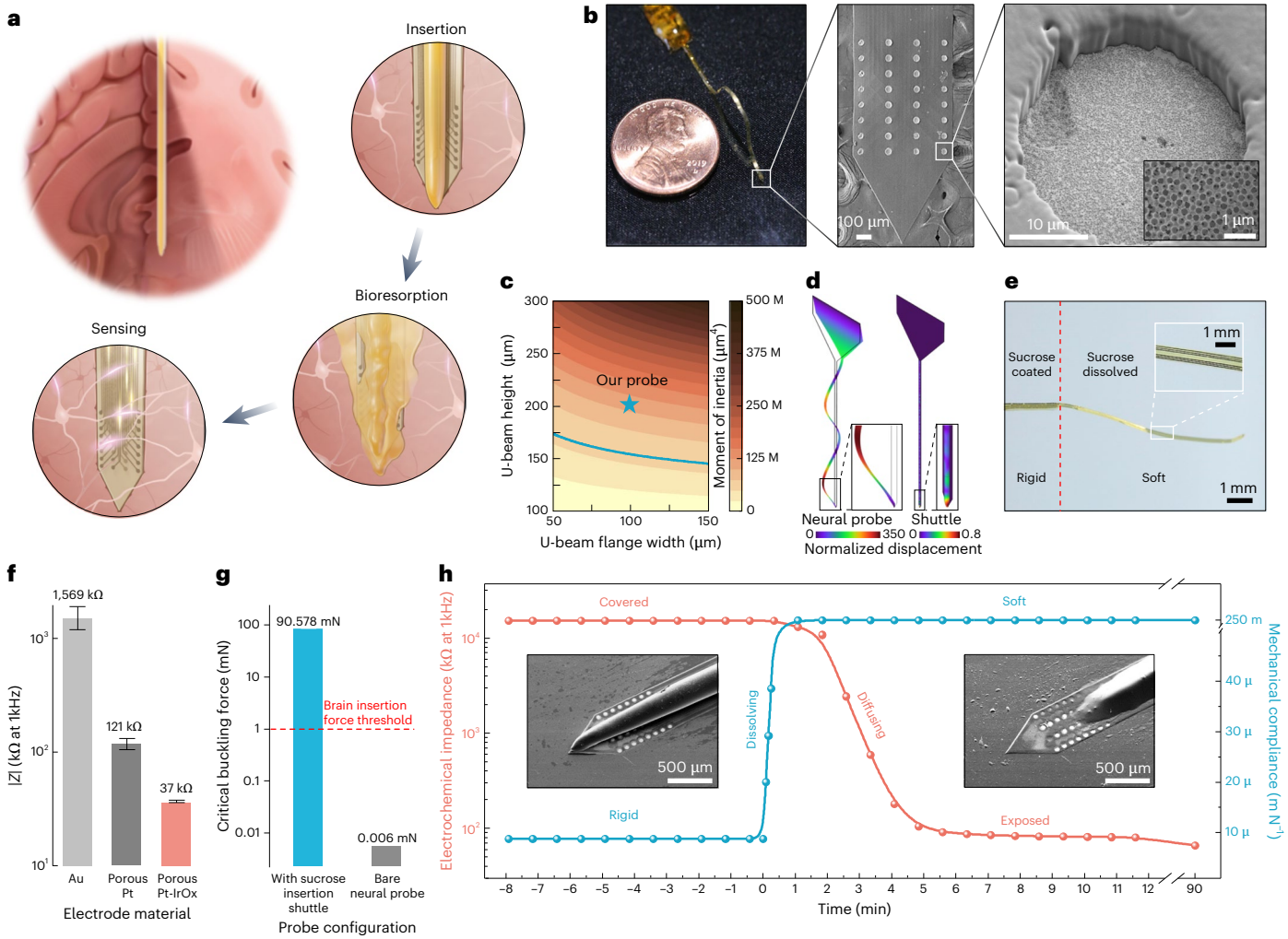

Fig. 3 | Flexible neural probe with a bioresorbable and mechanically transient sucrose insertion shuttle. a, Schematic illustration of the process where the shuttle guides the neural probe ('insertion') and dissolves ('bioresorption') to expose electrodes ('sensing'). **b**, Left: optical image of a neural probe after shuttle dissolution. Middle: SEM image of the microelectrode array. Right: SEM image of the 3D nanoporous microelectrode. The inset SEM image is a magnified view of the electrode. **c**, Theoretical value of the moment of inertia according to the geometrical parameters. The blue line represents the theoretical minimum threshold (~59.6 Mμm⁴) for a practical insertion force (50 mN). The star symbol represents the value for our neural probe. **d**, FEA showing the bending stiffness difference between the neural probe with (right) and without (left) the shuttle. **e**, Photograph highlighting the bending stiffness difference between the remaining part and dissolved region of the shuttle. The inset is a magnified view of the dissolved region. **f**, Electrochemical impedance (Z) at 1 kHz depending on the electrode material ($n = 4$ electrodes). Error bars represent the standard deviation of the data. **g**, Theoretical value of the critical buckling force of the neural probe with the shuttle and bare neural probe. **h**, Transient responses in the mechanical compliance of the neural probe and the electrochemical impedance of the electrode according to the elapsed time of insertion (time at 0 min) of the neural probe coated with the shuttle into a brain phantom (agarose gel, 0.6%). Inset SEM images show the configuration before (left) and after (right) sucrose dissolution.

The engineering design and configuration of the ferrite and copper layers of the stealthy neural recorder have a critical impact on the enhancement of wireless power efficiency by guiding the magnetic flux and noise reduction performance of the device. In this configuration, the ferrite sheet has a high magnetic permeability (~150) and a low magnetic loss (~5), which concentrates the external magnetic field and increases the magnetic flux passing inside the coil by enhancing magnetic coupling, resulting in a high-quality factor and efficiency for the coil (Fig. 4l–o, Extended Data Fig. 7a and Supplementary Fig. 12). Moreover, the copper sheet has a low magnetic permeability (~0.99), which protects sensitive electronic components and circuits from intensive magnetic flux near the coil, enabling precise measurement, by notably reducing background noise (Extended Data Fig. 7a), and reliable wireless communication (Extended Data Fig. 3c). Consequently, the stealthy neural recorder operates stably with wide variations not only in the relative distance, angle and bending curvature of the receiver coil from the repeater coil but also in the implant environment with biological fluids by virtue of efficient wireless power transfer (Extended Data Fig. 7b,c,e). Therefore, sufficient wireless power transmission in broad spaces allows seamless measurement of neural signals during the naturalistic behaviours of the monkey (Extended Data Fig. 8).

With these unique designs, materials and strategies in the wireless power transfer method for NHPs, the wireless power receiver coil implanted under the scalp has high efficiency, while the electromagnetic wave absorption by biological tissues is still low[28]. The finite element analysis (FEA) results support that the specific absorption rates (SARs) of the brain and scalp are 490 and 721 mW kg^{-1}, respectively, which are far below the safety threshold level of the Federal Communications Commission (FCC) guideline (CFR Part 1.1310; Fig. 4p and Supplementary Fig. 16a(left)). In addition, the subsequent temperature increment by electromagnetic wave absorption is negligible (Supplementary Fig. 16a(right)). The surface temperature of the encapsulated

https://doi.org/10.1038/s41551-024-01280-w

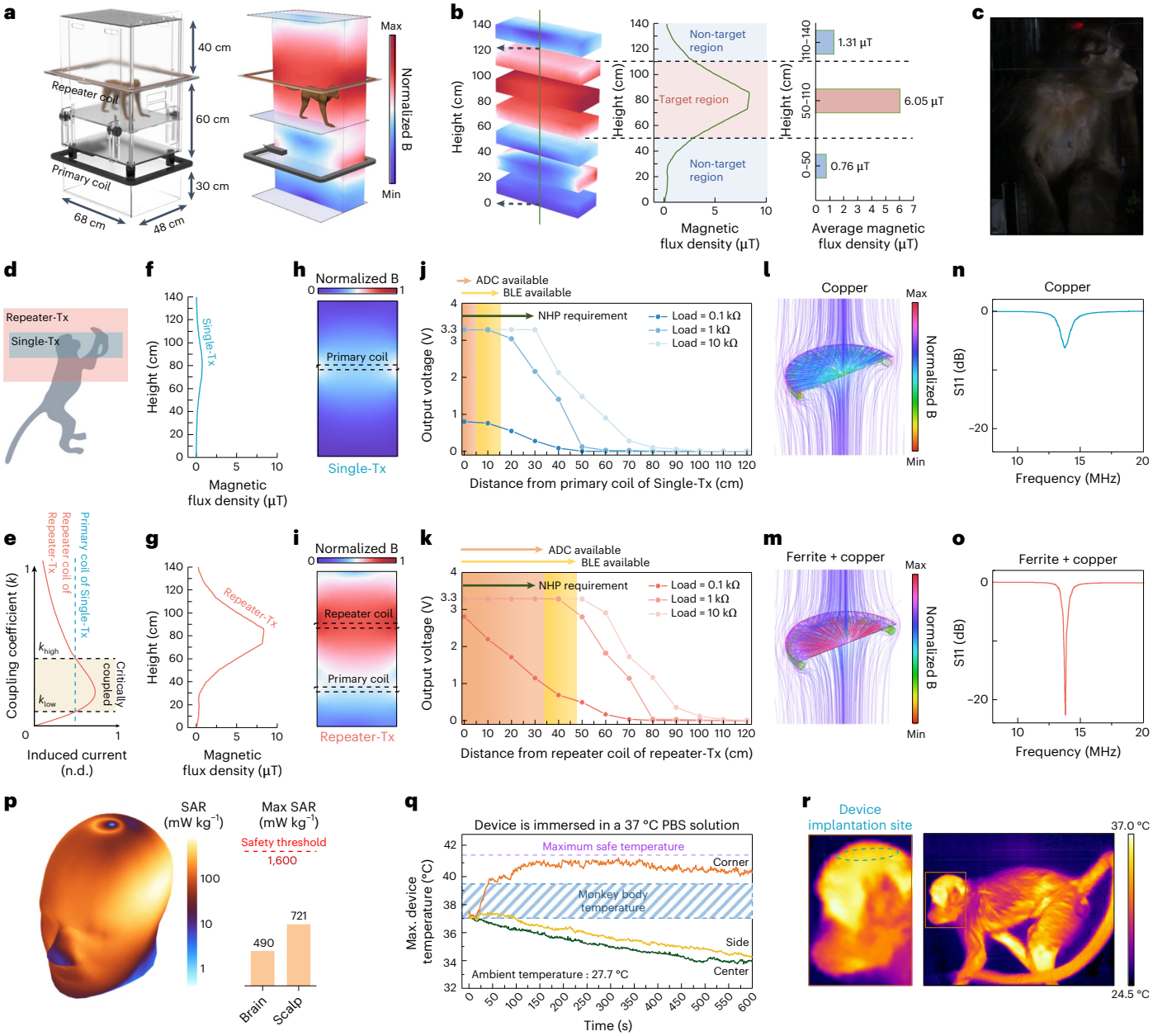

Fig. 4 | Long-range and high-efficiency wireless power transfer for NHPs via the Repeater-Tx system. a, Left: schematic illustration of the Repeater-Tx system. Right: FEA results of the magnetic flux density (B). **b**, Left: FEA results of the magnetic flux density (B) (primary coil power 12 W) along the height. Middle: simulated value along the centre line according to the height. Right: average simulated value in the defined regions. **c**, Photograph of the monkey with LED (red) on the implanted stealthy neural recorder under wireless power. **d**, Schematic illustration of the wireless power transfer range with a monkey. **e**, Analytical graph of current flowing through the repeater coil in the Repeater-Tx system according to the coupling coefficient (*k*). **f**–**i**, FEA results comparing the magnetic flux density (B) of the Single-Tx and Repeater-Tx systems in the cage: 1D plot along the centre line (**f**,**g**), 2D plot along the centre plane (**h**,**i**). **j**,**k**, Regulated output voltage of the stealthy neural recorder according to distance from each power source coil with different load values in the Single-Tx (**j**) and Repeater-Tx (**k**) systems. **l**,**m**, Streamlines of magnetic flux in the wireless power receiver depending on the absence (**l**) or presence (**m**) of a ferrite layer. **n**,**o**, RF behaviour depending on the absence (**n**) or presence (**o**) of a ferrite layer. **p**, Simulation results of the SAR of the brain and scalp where the head model is placed at the corner of the repeater coil (see detailed setup in Method and Supplementary Fig. 16). **q**, Maximum temperature profile of a device in a 37 °C PBS solution as a function of wireless power transfer time at the corner, side and centre position with respect to the repeater coil. **r**, Infrared image of the monkey body under wireless power.

neural recorder before implantation during wireless power increased to 34.4 °C (thermal imager, A665SC, FLIR) according to the distance from the repeater coil, which is lower than the body temperature of a monkey (37.0–39.5 °C[29]; Extended Data Fig. 7d). When experimenting with 37 °C phosphate-buffered saline (PBS) solution and pork tissue, the maximum temperature observed was 41.4 °C and 37.7 °C at the corner of the repeater coil (Fig. 4q and Supplementary Fig. 10). Infrared images of the monkey during wireless power transmission show that the heat generated by the implanted neural recorder is minimal, failing to penetrate the scalp. (Fig. 4r and Extended Data Fig. 7d).

Neurobehavioural recording and AI classification of eating behaviour phases in primates

Among diverse instinctive behaviours, studying eating behaviour in unconstrained conditions is crucial for understanding how organisms obtain essential nutrients through complex freely moving behaviours.

https://doi.org/10.1038/s41551-024-01280-w

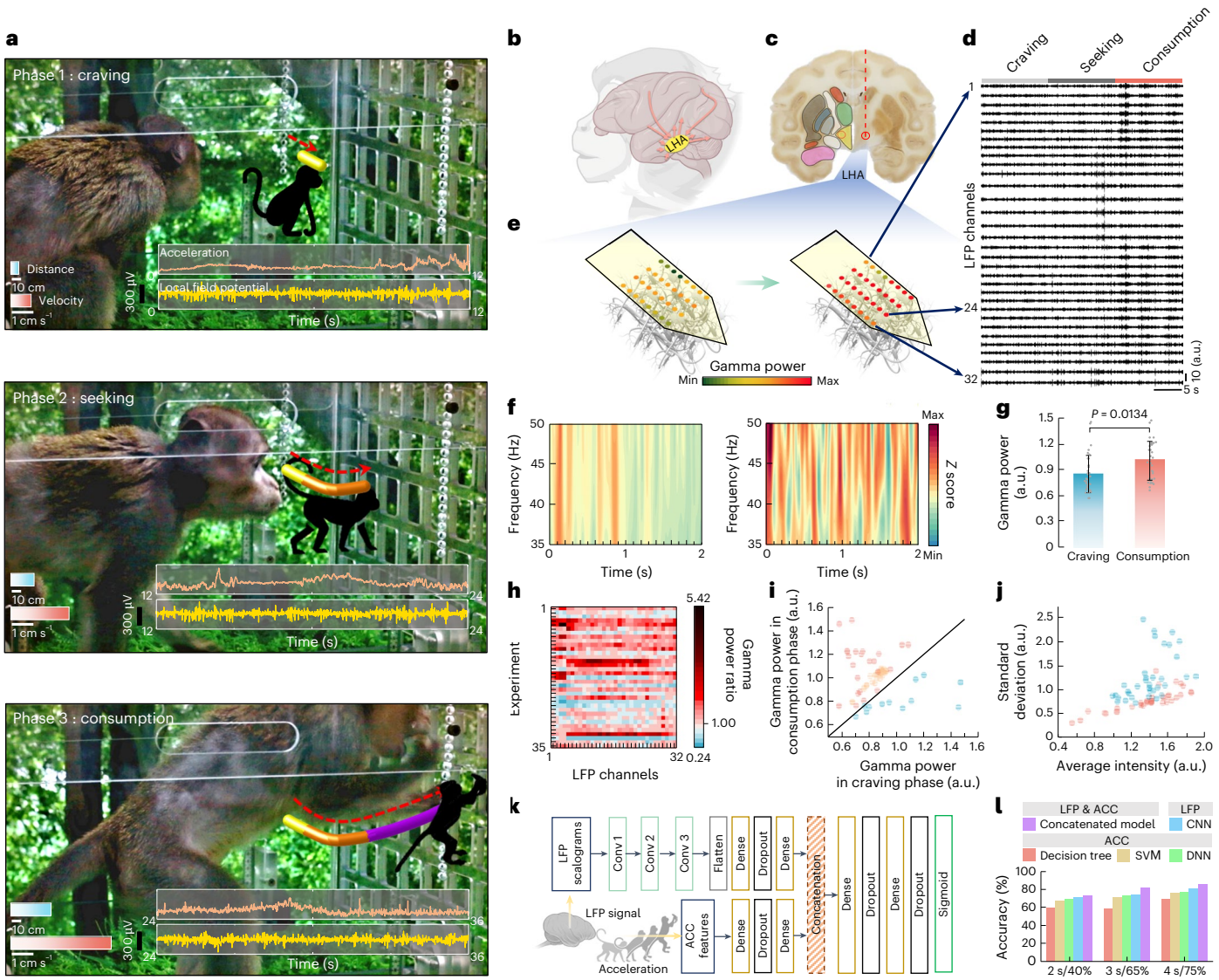

Fig. 5 | Monitoring of real-time neurobehavioural signals during eating behaviours, and phase classification. a, Chronophotography of monkey eating behaviour with real-time wireless neurobehavioural signal monitoring. **b**, Schematic illustration of the LHA neural circuit controlling eating behaviour. **c**, Histological image of the monkey brain coronal section showing the neural probe insertion track (dashed red line). Anatomical areas of brain subregions are outlined using the Paxinos Macaque Atlas (see Extended Data Fig. 6 for details). **d**, Representative filtered LFP traces (35–50 Hz) from 32 electrodes in the LHA. **e**, Heat map of averaged gamma (35–50 Hz) power of LFPs for each electrode in the craving (left) and consumption (right) phases during the experiments ($n = 35$). **f**, Averaged scalograms for all 32 electrodes in the representative experiment. **g**, Averaged gamma power of LFPs in the craving (blue) and consumption (red) phases during the experiments ($n = 35$). Two-sided Wilcoxon signed-rank test. Error bars represent the standard deviation of the data. **h**, Gamma power ratio (gamma power in consumption phase/gamma power in craving phase) across all experiments and channels. **i**, Gamma power distribution in the consumption versus craving phase during the experiments. Red and blue, averaged gamma power of each experiment in all electrodes. Orange, averaged gamma power of each electrode in all experiments. **j**, Feature extraction results of acceleration data in the craving (blue) and consumption phases (red) ($n = 35$). **k**, Proposed concatenated model architecture. **l**, Classification accuracies by different classifiers and input signal lengths with variable overlap ratios. The schematics in **b** were created with BioRender.com.

In the literature, we and others have classified eating behaviour into three phases: craving, seeking and consumption[30–32], which are encoded by distinct neural activities.

The hypothalamus serves as the primary controller of appetite. Among its regions, the lateral hypothalamus area (LHA) has been extensively studied for over 70 years[33–36] as the key orchestrator of eating in all animals, including NHPs and humans. In primates, several studies have observed neural activity changes of LHA neurons in response to feeding-related behaviour through electrode encoding in the LHA[37–39]. Therefore, recording LHA activity during multiphase eating behaviour is a logical and rational strategy for validating the functionality of a neural interface for freely moving NHPs (Fig. 5a,b).

The neural probe was stereotaxically inserted into the LHA of the monkey (Fig. 5c and Supplementary Figs. 4–6), and the monkey was moved to a customized wild-like wireless home cage for promoting naturalistic behaviour without any other wired constraints (Extended Data Figs. 6a and 9a,b). After a sufficient recovery period, local field potential (LFP) was recorded simultaneously on 32 channels (Fig. 5d,e). A total of 35 eating behaviour experiments were conducted. Each experiment lasted 36 s and was divided into phases every 12 s: craving, seeking and consumption. The experiments were performed for up to 4 weeks, while LFP signals and acceleration signals were transmitted using wireless communication, and the operation voltage was supplied by wireless power transfer (Extended Data Figs. 9c,d and 10b).

Then, recorded neurobehavioural signals were analysed through signal processing with embedded hardware and software algorithm for extracting distinct features related to each eating behaviour phase (Extended Data Fig. 10a).

The gamma band (35–50 Hz) of the LFP was extracted, followed by the calculation of scalograms and band power for further analysis (Fig. 5f). Analysis of LFPs from spatially mapped electrodes across all 35 eating behaviour experiments demonstrated that the averaged gamma power during the 12-s consumption phase was significantly higher than that during the 12-s craving phase (Fig. 5g and Supplementary Fig. 8). An increase in gamma power during the consumption phase was observed in most experiments and channels (Fig. 5h). This trend was consistent, whether averaging across channels for each experiment or averaging across all experiments for each single channel (Fig. 5i). To analyse the behavioural patterns of a freely moving monkey for eating behaviour, acceleration data from the accelerometer were collected for all eating behaviour experiments. Acceleration signals are often utilized to classify movement patterns in livestock or humans with several extracted features[40–42] such as movement variation, average intensity or standard deviation. In the craving phase which involves looking around or walking, a significantly higher standard deviation in acceleration signals was observed compared with the consumption phase ($P < 0.001$, paired t-test; Supplementary Fig. 9). This difference is attributable to the relatively static nature of motions, such as chewing or swallowing, that predominate during the consumption phase[43]. In addition, by integrating standard deviation alongside average intensity, clustering between the craving and consumption phases was observed, as depicted in Fig. 5j.

Several AI-based classifiers corresponding to decision tree, deep neural network (DNN), convolutional neural network (CNN), support vector machine (SVM) and the proposed concatenated model were applied to classify eating behaviour phases with the neural activity and behaviour patterns measured by the stealthy neural recorder. The calculated acceleration features and scalograms of LFP, commonly employed in neurobehavioural analyses[44,45], served as input data for classifiers. Acceleration features were the inputs for the decision tree, DNN and SVM, while scalograms of LFP were the inputs for the CNN (Extended Data Fig. 10f,g and Supplementary Table 2). Both acceleration features and scalograms of LFP were used as inputs for the proposed model. The proposed concatenated model is a multi-input classifier that employs DNN to extract information from acceleration features and CNN to analyse scalograms of LFP signals (Fig. 5k). By combining these extracted features through a concatenated layer, the model effectively classifies eating behaviour phases (see Supplementary Table 3 and Extended Data Fig. 10h for details of layer information).

To account for the continuous behaviour of NHPs, 12-s signals measured for each phase were segmented with overlaps and features were calculated (Extended Data Fig. 10c). We compared several AI-based classifiers with 5-fold cross-validation to find a high-performance classifier and optimized input neurobehavioural signals determined by a segmented time window and overlap ratio. Among the various methods and input data employed, a deep-learning model incorporating both LFP and acceleration data yielded the highest average accuracy of 86.33% when the neurobehavioural signals were segmented with a 4-s time window and 75% overlap (Fig. 5l, Extended Data Fig. 10d,e and Supplementary Table 4). This result suggests that the proposed model using both LFP and acceleration data recorded by the stealthy neural recorder is a feasible and effective approach for classification of eating behaviour phases.

Discussion

We have shown that our stealthy neural recorder enables real-time wireless monitoring of neurobehavioural signals and the analysis of biomedical indicators of naturalistic behaviours in NHPs. The neural recorder represents a compact fusion of functional layers with a wireless embedded system, stealthily and accurately streaming neurobehavioural signals without impinging on the instinctive behaviour of the monkey. The long and flexible neural probe was accurately inserted into the LHA region using a bioresorbable sucrose insertion shuttle, which enabled minimally invasive recordings of neural signals in deep brain regions. Further enhancing the stealth and operability of our neural recorder, we employed a repeater-coil-based wireless power transfer. This ensured sufficient and stable operation of the battery-free device across a broad range of uncontrolled primate movements without causing disturbance to the monkey. Through a month-long eating-behaviour experiment, we used the neural recorder to record LFP signals, revealing significant differences in gamma power across different phases of eating behaviour. Using biomarkers extracted from recorded neurobehavioural signals, we developed a deep-learning model that achieved an 86.33% average classification accuracy in distinguishing eating behavioural phases. The stealthy neural recorder surpasses the constraints of previously reported neural recording devices and offers an advanced integrated-device solution for the study of the innate behaviour of primates in an uninhibited manner. We believe that the neural interface opens up possibilities for extensive studies of complex neural circuitry in NHPs and for the study of human brain disorders.

Methods

Design, fabrication and electronic circuits of the stealthy neural recorder

The top module comprised a litz coil for wireless power induction, a flexible ferrite sheet for magnetic flux concentration and a rectifier circuit. A litz wire (0.12 mm diameter, 10 strands) formed a litz coil (6 turns) that received wireless power by winding along the outer periphery of a flexible ferrite sheet (IBF15-100DD125X125, TDK, relative permeability $\mu' = 150$, 0.1 mm thickness) coated with acrylic adhesive while minimizing spacing between wires. A custom-designed flexible printed circuit board for rectification was placed inside the litz coil, bonded to the flexible ferrite sheet and soldered to the litz coil to make electrical connections. Litz coils have higher performance than planar coils and are more flexible than solid coils, making them suitable for application to implantable devices (Supplementary Fig. 15). A parallel capacitor (16–18 pF) defined a resonance state at 13.56 MHz, as measured using a vector network analyser (E5071C, Keysight). A full-wave rectifier based on four Schottky diodes (BAS40T-05 and BAS40T-06, Diodes Incorporated) and two smoothing capacitors (4.7 µF) rectified the harvested wireless power. A Zener diode (PDZVTFTR36B, ROHM Semiconductor) provided overvoltage protection, and a low-dropout regulator (AP2204k-3.3TRG1, Diodes Incorporated) stabilized the power at 3.3 V to charge a supercapacitor (XH414HG-IV01E, Seiko Semiconductors) that operated the entire embedded system. The bottom module comprised circuits for neurobehavioural signal measurement and wireless communication. The raw neural signal was passed through an RFI filter ($fc = 5$ kHz) to suppress magnetic interference from the RF field. A biopotential amplifier (RHD2132, Intan Technologies) amplified and filtered neural signals and performed analogue-to-digital conversion (ADC). An accelerometer (ADXL337, Analogue Devices) measured acceleration along three orthogonal axes. A Bluetooth Low Energy System-on-Chip (BLE SoC, QN9080SIP, NXP Semiconductors) system with a built-in 2.4 GHz antenna wirelessly transmitted data packets, including neural signal, acceleration and system power level, to a smartphone (Android) or laptop in real time. A flexible printed circuit (FPC) connector (503480-3200, MOLEX) provided simple and multiple electrical connections with the neural probe. The fabricated top module and the bottom module were attached with double-sided Kapton tape to form a sandwich structure, and jumper wires (AWG34) electrically linked the two modules. The reference and ground provided a stable electrical baseline by soldering jumper wires (AWG34) and connecting the Pt wire (0.1 mm diameter) at the end.

Fabrication of the neural probe and electrodes

Fabrication began by spin-casting a layer of poly(methyl methacrylate) (PMMA; ~1 µm thickness, Microchem) to form a thin sacrificial layer on a silicon wafer substrate. The bottom layer of the neural probe was formed by spin-casting PI (1–3 µm thickness, Sigma–Aldrich), depositing thin layers of metal by sputtering (Cr/Au; 7 nm/200 nm thickness), performing photolithography, wet etching and spin-casting another layer of PI. The top layer of the neural probe was fabricated by depositing additional thin layers of metal by sputtering (Cr/Au; 7 nm/200 nm thickness), performing photolithography, wet etching and spin-casting another layer of PI, followed by oxygen reactive ion etching (30 mTorr, 20 sccm, O_2, 150 W, 35–45 min) of the PI layers (Extended Data Fig. 5a). Dissolving the PMMA by immersion in acetone for 30 min at 85 °C enabled release with water-soluble tape (Water-Soluble Wave Solder 5414, 3M).

Surface modification of neural electrodes

Laminating a polyethylene terephthalate (PET) film coated with a thin layer of polydimethylsiloxane (PDMS) onto a glass substrate ($5 \times 50 \times 0.7$ mm^3) enabled temporary transfer printing of the neural probe with van der Waals forces after dissolving the water-soluble tape in warm water. Electrochemical cleaning was performed by immersion in a potassium hydroxide (KOH; 50 mM, Sigma-Aldrich) and hydrogen peroxide (H_2O_2; 25%, Sigma-Aldrich) solution at a 3:1 volume ratio, followed by a potential sweep in a potassium hydroxide (KOH; 50 mM, Sigma-Aldrich) solution between −0.2 V and −1.2 V (vs Ag/AgCl) at a scan rate of 50 mV s^{-1} to remove residue on the gold electrodes. Dilution of monodispersed polystyrene nanospheres (PS; ~220 nm diameter, Sigma-Aldrich) with Millipore water (18 MΩ) followed by sonication (~5 min) formed a colloid solution (0.5 wt %). Drop drying 0.5 µl of colloid solution on gold electrodes of the neural probe placed on an 80 °C hotplate (~1 min) formed a high-yield assembly of monodispersed PS particles on the electrodes. After the PS stacking process, 3D porous Pt electrodes were produced by electrodeposition with a chloroplatinic acid solution (H_2PtCl_6; 50 mM, Sigma-Aldrich) at a constant current density of 2 mA cm^{-2} for 3,000 s, followed by dissolving PS particles in tetrahydrofuran (THF; DAEJUNG) for 24 h. Further electrodeposition based on the Yamanaka method[46] was carried out by chronoamperometry at +0.6 V (vs Ag/AgCl) for 300 s and addition of a thin iridium oxide (IrOx) layer on the surface of the electrode pores.

Stamp printing of the sucrose needle

A mould with a debossed pattern was developed by spin casting and photolithography of photocurable epoxy (SU-8 2100, Kayaku Advanced Materials) on a silicon wafer. Casting PDMS (Dow Corning, Sylgard 184) onto the developed mould and peeling off the PDMS layer yielded a soft polymer stamp with an embossed pattern for stamp printing. A silicon wafer coated with a PDMS layer (~500 µm) was placed on a hotplate set at the melting temperature of sucrose (180–200 °C) until the sucrose was completely melted. Careful contact of the PDMS stamp with melted sucrose defined the sucrose to be coated on the embossed pattern. Peeling off the PDMS stamp from the patterned sucrose produced a bioresorbable U-beam-shaped insertion shuttle.

Integration, assembly and encapsulation of the stealthy neural recorder

The FPC connector and the contact pad of the neural probe were electrically connected by adjusting the thickness (~0.3 mm) of the head part of the neural probe with Kapton tape. The entire device was encapsulated by casting PDMS onto the centre-aligned device inside the circular mould partially filled with PDMS. On the basis of the curvature of the skull measured in the monkey by magnetic resonance imaging (MRI), a 3D-printed curved polycarbonate (PC) support was fabricated and bonded to the base of the device with silicone elastomer (Ecoflex 00-35, Smooth-On) to minimize pressure on the inside of the scalp. Chemical vapour deposition (Lavida 110, FEMTO SCIENCE) of Parylene-C (18 µm; NURITECH) was used to encapsulate the device with a conformal coating. After peeling off the PET film under the neural probe, a sucrose insertion needle was aligned and bonded to the neural probe under appropriate moisture and heat exposure.

Wireless communication, device function and system operation

All in vitro and in vivo experiments were conducted with real-time wireless communication under battery-free operation. Commercial packages, including the MCUXpresso Software Development Kit (SDK) by NXP and Bluetooth Low Energy (BLE) 5.0, served as tools for building embedded software for the overall system. An embedded microcontroller ran a callback function to capture the values of each sensor (biopotential amplifier, accelerometer and system power level sensor) at a desired sampling rate (Extended Data Fig. 2; Mode 1, 2 and 3: 11 kSa s^{-1}; Mode 4: 0.9 kSa s^{-1}) with an embedded hardware timer (32 kHz) at a regular interval depending on the firmware mode. The embedded software was programmed to transmit over the air through the BLE protocol when the packet data reached 244 bytes. A custom Android-based application was used to receive and display real-time signals. A customized MATLAB 2021b (Mathworks) code was used for further signal processing and analysis. Bidirectional wireless communication allowed for the simultaneous execution of system controls, including firmware mode change, light-emitting diode (LED) control, electrode channel change and system reset, while receiving real-time signals. The LED functions primarily as a visual indicator for confirming wireless power reception efficiency during device development and immediate post-implantation diagnostics. It also serves to verify the functional status of the embedded device's microcontroller unit (MCU) by signalling on/off states. Experimentally, the LED signifies successful command reception, with a specific blink pattern indicating channel selection in high sampling rate signal modes. For spike detection, the LED illumination provides a real-time visual spike rate metric, which is essential for behavioural correlation studies, without affecting the primate subject. This system is designed to replace auditory feedback typically used in neural recording, facilitating unobtrusive behavioural observations.

In vitro test

To ensure reliable and efficient monkey in vivo experiments, we assessed the performance of the stealthy neural recorder under various conditions using in vitro experiments with a neural simulator (Extended Data Figs. 2d, 7a(left) and 8a,b). The neural simulator (FB128, TDT) was interfaced with a multichannel connector (ZIF-Clip connector, NeuroNexus) connected with microwires. We either directly connected wires to the stealthy neural recorder's input connector or immersed a single microwire in PBS (0.05 M, pH 7.4, Sigma-Aldrich) containing the recorder linked to a neural probe. For authenticity, all in vitro experiments were set up within an actual monkey wireless power home cage, emulating the genuine in vivo environment as closely as possible. To mirror the in vivo experimental paradigm, including device operation and data acquisition, we powered the device wirelessly, avoiding battery usage, and collected data through wireless communication, ensuring a completely tetherless operation. Operating the neural simulator in normal mode, we measured signals across the full spectrum of neural frequencies. This allowed us to evaluate the recorder's capacity to filter the neural signals within the desired frequency bands as programmed in its firmware.

Noise immunity test under wireless power transmission

To assess the noise introduced by wireless power transmission, the neural simulator (FB128, TDT) was electrically connected with the stealthy neural recorder via a dedicated cable connection. For static motion analysis, spike activities were recorded for 10 s at intervals of 10 cm, ranging from 20 cm below to 40 cm above the repeater coil, to quantify noise fluctuations as a function of elevation. For dynamic

motion analysis, the recorder was vertically displaced at velocities of 4 cm s^{-1} and 60 cm s^{-1}, and spikes were recorded for 10-s intervals while traversing from 20 cm below to 40 cm above the repeater coil. Data acquisition was executed at a sampling frequency of 11 kHz, and the obtained signals were wirelessly relayed to a laboratory computer via BLE. Signal-to-noise ratio (SNR) was calculated as $SNR_{dB} = 20 \times \log_{10}(V_{RMS\ signal}/V_{RMS\ background\ noise})$, where $V_{RMS\ signal}$ and $V_{RMS\ background\ noise}$ are the root mean square values of the voltage of the detected neural spike and preceding background noise of equal duration, respectively. A customized MATLAB code was utilized for spike detection and for applying a band-pass filter with a frequency range of 300–5,000 Hz.

FEA for mechanical characterization of the neural probe

The commercial software COMSOL was used to analyse the buckling of the neural probe with the sucrose insertion shuttle and the stretching of the serpentine interconnect in the upper part of the neural probe. The 3D solid mechanics module and linear buckling analysis defined the mechanical behaviours of the neural probe. In the buckling analysis, the critical buckling force derived from linear buckling analysis provided a deformed configuration and displacements for comparison with and without the sucrose insertion shuttle. To evaluate the stretchability of the serpentine interconnect of the neural probe during surgical implantation, the device was rotated at different angles to examine the stress distribution on the neural probe. The elastic modulus and Poisson's ratio values used in simulations were as follows: $E_{neural\ probe} = 3.1$ GPa, $\nu_{neural\ probe} = 0.43$, $E_{sucrose} = 35.7317$ GPa, $\nu_{sucrose} = 0.3$.

Dynamic mechanical analysis for the transient mechanics of the sucrose-coated neural probe

A dynamic mechanical analyser (DMA 850, TA Instruments) allowed measurement of the bending stiffness of the sucrose-coated neural probe using a 3-point bending clamp. The samples were inserted into a brain phantom (agarose gel, 0.6%) every 5 s and then dried for measurement. The frequency of loading was set to 1 Hz and the temperature of the DMA chamber was constant at 23 °C. The mechanical compliance was calculated as the reciprocal of the measured bending stiffness.

Electrochemical impedance spectroscopy (EIS) of 3D nanoporous electrodes

Potentiostatic EIS by a potentiostat (Interface 1010E, Gamry Instruments) was used to measure the electrochemical impedance in PBS (0.05 M, pH 7.4, Sigma-Aldrich) with a 10-mV amplitude AC signal. In the electrochemical impedance measurement according to the process of surface modification of neural electrodes, the impedance was measured from 0.1 Hz to 100 kHz. On the other hand, the impedance measurement of the electrode according to sucrose dissolution was performed at 1 kHz to prevent additional dissolution during measurement.

Wireless power transfer system coupled with repeater coil

The RF power module (LR2500-A, Feig Electronics) drove a large-loop primary coil (ANT800600-DA, Feig Electronics) placed under the primate home cage. Dedicated software (ISO start, Feig Electronics) maintained impedance matching of the coil tuner (DAT, Feig Electronics) through a USB cable connected to the host computer. The repeater coil (60 × 80 cm^2) was fabricated by winding a litz wire (0.12 mm diameter, 100 strands, 6 or 9 turns), and tuned with parallel capacitors in a similar way as described before in the device fabrication. The distance between the primary coil and the repeater coil was selected to maximize the monitored value of the power metre (WT210, Yokogawa Electric) connected to the power module while changing the distance within the range estimated by the analytical model. Since the condition for maximum wireless power transmission varied according to changes in the surrounding environment, such as the presence of primates or metal objects near the coil, the tuning of the repeater coil and the distance between the two coils were adjusted depending on the situation. Finally, a footrest for the monkey was adjusted to position the monkey's head at the height of the repeater antenna to obtain the maximum wireless power range during the entire experiment.

Electromagnetic simulation of wireless power transfer

Commercial software COMSOL allowed simulation of the magnetic flux density inside the cage surrounded by loop coils using FEA to study the magnetic performance of the Repeater-Tx system. Lumped elements matched the resonance frequency (13.56 MHz) by setting the capacitor values connected on both coils (primary coil and repeater coil). Lumped ports determined the input RF power (~12 W) and characteristic impedance (50 Ω) of the primary coil. A physics-controlled mesh (tetrahedron elements) together with a cuboid surface (10 × 10 × 14 cm^3) as the radiation boundary ensured computational accuracy. In the simulation of the wireless power receiver according to the ferrite and copper layers (each 100 μm thickness), a coil (copper, 3 cm radius) tuned to the resonance frequency was placed in the centre at the same height as the repeater coil. The relevant material parameters were: relative permeability $\mu' = 150$, $\mu'' = 5$ for the ferrite layer, and relative permeability $\mu_r = 0.999994$ for the copper layer. The other material parameters used were obtained from the material library provided by COMSOL. Simulations of the SAR and the resulting temperature effect on the head were performed using an electromagnetic wave and bioheat transfer module from the COMSOL RF module. The relative permittivity (ε_r) and electrical conductivity (ρ) were as follows: $\varepsilon_{r,scalp} = 177.1$, $\varepsilon_{r,brain} = 208.3$, $\rho_{scalp} = 0.384$ S m^{-1}, $\rho_{brain} = 0.252$ S m^{-1}.

Electromagnetic characterization of coils depending on the implant environment

To implant the stealthy neural recorder on the skull of monkeys, bending of the device is necessary to minimize pressure on the scalp; therefore, the characteristics of the coil against bending should be evaluated in advance. The bending of the device according to the range of curvature of the monkey skull, measured using a computed tomography (CT) image, shifts the resonant frequency and lowers the quality factor of the coil (Extended Data Fig. 7c,e(left)). In addition, biological tissues and fluids, which have higher permittivity than air, existing around the implanted device increase the effective capacitance of the coil and lower the resonant frequency. Over-tuning the coil by as much as the shifted resonant frequency measured by immersing the device in saline solution (pH 7.4) prevents performance degradation of the coil in the in vivo environment after device implantation and ensures long-term device operation (Extended Data Fig. 6e(middle)). During long-term implantation, the quality factor (Q) and resonance frequency of the device were assessed by measuring the scattering parameter of the coil every week on the monkey head using a vector network analyser (E5071C, Keysight) to evaluate the operating performance. One-month implant results in a monkey showed no further change in the resonant frequency as weeks passed after implantation, and the quality factor of the coil increased as the swelling subsided at the surgical implantation site (Extended Data Fig. 6e(right)).

Surgical implantation

The stealthy neural recorder was first sterilized with ethanol solution and then fixed to a stereotaxic insertion rod with silicone adhesive (Ecoflex 00-35, Smooth-On). Reference and ground wires were wound around the skull screws and inserted into the skull hole to provide a stable electrical baseline. For vertical insertion of the neural probe, heat was applied to the upper portion of the sucrose coating to partially dissolve the sucrose, with the probe allowed to hang vertically. After the probe was moved to the insertion coordinates specified by MRI, the probe was inserted at a constant speed (1 mm s^{-1}). The remaining sucrose on the probe with the device was dissolved with warm saline after the probe was inserted into the desired depth. The device was

carefully detached from the stereotaxic frame, positioned and fixed to the skull with cyanoacrylate adhesive (Henkel). Then, the space between the device and the skull was filled with biocompatible silicone (Kwik-Sil, World Precision Instruments) to prevent infiltration of biological fluids. Scalp suturing and additional sterilization of the suture completed the surgical implantation process.

Phases of eating behaviour

For the eating behaviour states, we defined three phases: Phase 1: 'Craving', the phase when the monkeys are placed under fasting conditions and are searching for food in the primate home cage. Phase 2: 'Seeking', the phase when the monkey recognizes and approaches foods (such as apples, bananas and cranberries) that are introduced beyond the monkeys' reach by the experimenter. Phase 3: 'Consumption', the phase when the monkey obtains and consumes food through biting, chewing and swallowing. Twelve-second periods were sampled for analysis in each phase.

Neurobehavioural signal recording of eating behaviour in NHPs

After a recovery period of at least 1 day after the surgical implantation of the stealthy neural recorder, the monkey was moved to a wireless-power home cage. The monkey was allowed an additional recovery period of 1 week. This was followed by a series of eating behaviour experiments spanning 4 weeks. These experiments were conducted every week within the customized wireless-powered home cage. The food for the eating behaviour test was selected from food pellets, cranberries, apples and bananas according to the monkey's preference. The experimenter monitored the time to distinguish the three stages of the eating behaviour experiment, transitioned stages every 12 s for a total of 36 s and collected neurobehavioural signals using a smartphone or laptop. All neurobehavioural signal recording of eating behaviour was performed in situations where monkeys behaved instinctively. All in vivo experiments were video recorded with five cameras, including front, side and top views, for further behaviour observations.

Neurobehavioural signal analysis

LFP signals and acceleration of the monkey head were simultaneously recorded at a sampling rate of 925 Hz and 308 Hz, respectively. After common average referencing, the 4th-order Butterworth band-pass filter was applied to denoise motion artefacts as well as power line artefacts and extract gamma waves from the LFP signals, with a specified frequency band of 35–50 Hz. Then, the 36-s filtered LFP signals were divided into 12-s segments after z-normalization. The acceleration was also band-pass filtered (0.5–10 Hz) and subsequently z-normalized. The acceleration magnitude was calculated before the feature extraction. Then, the 36-s filtered acceleration signals were divided into 12-s segment. To assess significant differences in gamma power between consumption and craving phases, the gamma power of the 32 channels measured in each experiment was averaged, followed by Wilcoxon signed-rank test. The alpha level was set at $P < 0.05$. In addition, signals measured in each trial and channel were averaged and compared across all 35 experiments for each channel. The acceleration magnitude was calculated before feature extraction. The average intensity used for feature extraction is defined as

$$\text{Average Intensity} = \frac{1}{N}\sum_{i=1}^{N} a_{\text{mag},i}, \tag{1}$$

where N is the number of samples and a_{mag} is the acceleration magnitude. The standard deviation, employed as another feature extraction, is defined as follows.

$$\text{Standard deviation} = \sqrt{\frac{1}{N}\sum_{i=1}^{N}\left(a_{\text{mag},i} - \frac{1}{N}\sum_{i=1}^{N} a_{\text{mag},i}\right)^2}. \tag{2}$$

The movement variation was calculated as follows where a_x, a_y and a_z represent the acceleration data on the X-axis, Y-axis and Z-axis, respectively.

$$\text{Movement variation} = \frac{1}{N}\left(\sum_{i=1}^{N-1}|a_{x,i+1} - a_{x,i}| + \sum_{i=1}^{N-1}|a_{y,i+1} - a_{y,i}| + \sum_{i=1}^{N-1}|a_{z,i+1} - a_{z,i}|\right). \tag{3}$$

3D reconfigured motion tracks of the monkey head were computed via double numerical integration with the trapezoidal rule. All signal analyses were performed using MATLAB 2022b (MathWorks) and Excel Microsoft 365 (Microsoft).

Neural spike analysis

Neural signals of the rat primary motor cortex were recorded at a sampling rate of 11 kHz. The signals were filtered from 300–3,000 Hz with the 4th-order Butterworth band-pass filter. The detected spikes from the electrodes were sorted via two-dimensional principal component analysis and k-means clustering. All spike analyses were performed using a customized MATLAB 2022b (MathWorks) code.

Eating behaviour classification using AI

The 12-s craving and consumption phases from experiments exhibiting higher gamma power during the consumption phase compared with the craving phase were segmented for behavioural classification of NHPs using neurobehavioural signals measured by the stealthy neural recorder. Segmentation was performed using varying window sizes and different percentages of overlap between adjacent windows (4 s/75%, 3 s/65%, 2 s/40%), ensuring that the 12 s could be divided into equal parts. Machine learning and deep-learning techniques were performed in TensorFlow (Google) and validated for accuracy using 5-fold cross-validation. Scalograms of LFP signals were obtained through continuous wavelet transform (CWT) using Morlet wavelet to provide time-frequency representations that can be employed as input features for subsequent classifiers. A DNN utilized for acceleration features consisted of two dense layers with 16 and 8 nodes, while a CNN for LFP signals comprised three convolution layers and two dense layers. Moreover, the concatenated model using both LFP and acceleration signals comprised one model with three convolution layers and two dense layers for LFP analysis, and another model with two dense layers for acceleration analysis connected by a concatenation layer. Then, the concatenated layer was linked to two additional dense layers for the purpose of classifying eating behaviour. Also, Adam optimizer and binary cross-entropy were used to train the model.

Animals

Sprague–Dawley rats (wild-type, 8-week-old male, 250–280 g; KOATECH, Korea) were used for this study. Rats were maintained under a 12 h light/dark cycle with ad libitum access to standard laboratory chow and drinking water. All experimental procedures were approved by the Animal Care and Use Committee of the Daegu Gyeongbuk Institute of Science and Technology (DGIST, IACUC 21081101-0002).

Cynomolgus monkeys (*Macaca fascicularis*) were obtained from Suzhou Xishan Zhongke Laboratory Animal Company and housed in individual indoor cages at the National Primate Research Center (NPRC) of the Korea Research Institute of Bioscience and Biotechnology (KRIBB), as described previously[47]. Monkeys were fed twice daily with commercially available monkey feed (Harlan) supplemented with various fruits and water ad libitum. The controlled environmental conditions were as follows: temperature, 24 ± 2 °C; relative humidity, 50 ± 5%; 12 h light/dark cycle. All experimental procedures described involving animal care and the use of NHPs were approved by the KRIBB Institutional Animal Care and Use Committee (KRIBB-AEC-21102). Experimental procedures were performed in accordance with national guidelines and complied with the Guidelines for the Care and Use of

Laboratory Animals. All animals were monitored at least twice daily and were provided appropriate veterinary care by trained personnel. The health of animals was monitored by the attending veterinarian, consistent with the recommendations of the Weatherall Report. Animal health monitoring was performed using microbiological tests, including tests for B virus, simian retrovirus, simian immunodeficiency virus, simian virus 40 and simian T-cell lymphotropic virus, once a year, as described previously[48].

Surgical procedures

Rats were anaesthetized via intraperitoneal (i.p.) injection of ketamine (100 mg kg^{-1}) and xylazine (5 mg kg^{-1}). During stereotaxic surgery, the rats were placed on a stereotaxic frame and fixed by ear bars (David Kopf). The neural probe and stainless needle were injected into the cerebral cortex (coordinates from bregma: −2.4 mm AP, ±1.8 mm ML, −2 mm DV). A 30-gauge stainless needle (300 μm outer diameter) was used as a negative control. The neural probe (diameter of 200–300 μm) and stainless needle insertion was controlled using a motorized stereotaxic robot system (Neurostar) mounted on a stereotaxic frame. After insertion, the neural probe and stainless needle were kept in the targeted region for 5 min and fixed with dental cement for a period of 7 days for the long-term experiment.

For in vivo recording, rats were anaesthetized with ketamine (100 mg kg^{-1}) and xylazine (5 mg kg^{-1}) via intramuscular injection (i.m.). The placement of the probe was managed using a stereotaxic system (NAN Instruments) while the rats were fixed by ear bars (David Kopf) in the stereotaxic frame. The neural probe was inserted into the primary motor cortex (coordinates from bregma: +2.0 mm AP, +2.5 mm ML, −1.3 mm DV).

Monkeys were initially anaesthetized via i.p. injection of a cocktail mixture of ketamine (5 mg kg^{-1}) and atropine (0.02 mg kg^{-1}) and fixed in the prone position using a custom-built CT- and MRI-compatible stereotaxic frame under isoflurane-induced anaesthesia (1.5% in 2 l min^{-1} oxygen). After confirmation of head restraint within the stereotaxic frame, pre-operative MRI scanning was performed as a baseline reference for targeting the brain region. Baseline images were used to determine the stereotaxic coordinates of a targeted brain region: the lateral hypothalamic area. A fiducial MRI marker was used as a precise reference point. A burr hole was created with a medical drill, ~5–7 mm in diameter. The neural probe coated with sucrose insertion shuttle was inserted into the target region using a motorized stereotaxic robot system and left for 10 min to dissolve the sucrose microneedle. Vital signs, including heart rate, SpO_2 and body temperature, were monitored during anaesthesia throughout all surgical procedures. Enrofloxacin (5 mg kg^{-1}) and ketoprofen (2 mg kg^{-1}) were administered after stereotaxic surgery. Post-operative CT and MRI were performed to confirm neural probe localization.

MRI

During brain MRIs, monkeys were anaesthetized with 2% isoflurane in 99.9% oxygen (2 l min^{-1}) and immobilized in a sphinx position in a custom-built stereotaxic frame. Inhaled CO_2 level, O_2 saturation, pulse, respiration rate and body temperature were monitored continuously, and body temperature was maintained with a warm blanket surrounding the animal. The MRI experiment was conducted on a 3.0-T MRI scanner (Achieva 3.0 T, Philips Medical Systems) with a 32-channel head coil[49]. Three-dimensional coronal T1-weighted images were acquired using the Turbo Field Echo sequence, with the following parameters: TR/TE = 14/6.9 ms, 150 × 150 field-of-view, matrix size 300 × 300, 1.0 mm slice thickness, −0.5 mm slice gap, flip angle 8°, acquisition voxel size 0.5 × 0.5 × 0.5, number of slice 200, average 4.

Tissue processing and histological analysis

Animals were perfused with PBS followed by 4% paraformaldehyde under deep anaesthesia. The whole brain was removed from the skull, washed with cold PBS and post fixed in 4% paraformaldehyde for 24 h at 4 °C. The monkey brain was sliced into 8-mm coronal slices using a custom-built monkey brain slicer. The rat whole brain and monkey brain slices were immersed in 15% sucrose-PBS solution until the tissue sank and then transferred to 30% sucrose-PBS solution. After brain dehydration, brain tissue was embedded in optimal cutting temperature (OCT) compound, and the embedded brain material was frozen at −80 °C. For Nissl staining, brain tissues were mounted on gelatin-coated slides and stained with 0.1% cresyl violet acetate (Sigma-Aldrich). For immunofluorescence staining (Supplementary Fig. 5), monkey brain tissues were blocked for 1 h with 5% normal goat serum by free floating and then incubated for 12 h at 4 °C with the following primary antibodies: polyclonal rabbit glutamic acid decarboxylase 67 (GAD67, 1:200, GTX101881, GeneTex), polyclonal rabbit vesicular glutamate transporter 2 (VGLUT2, 1:200, GTX54871, GeneTex) and polyclonal chicken neuronal nuclei (NeuN, 1:500, GTX00837). Brain tissues were incubated at room temperature in darkness for 1 h with the following fluorescence conjugated secondary antibodies: Alexa Fluor 594 goat anti-rabbit (1:1,000, 20112, Biotium) and Alexa Fluor 488 goat anti-chicken (1:1,000, ab150169, Abcam). Brain tissues were mounted and coverslipped with 4, 6-diamidino-2-phenylindole (DAPI) VECTASHIELD HardSet antifade mounting medium (H1500, Vector Laboratories) for nuclei counterstaining, and images were acquired using an Olympus BX51 microscope.

Reporting summary

Further information on research design is available in the Nature Portfolio Reporting Summary linked to this article.

Data availability

The main data supporting the results in this study are available within the paper and its Supplementary Information, and also from figshare at https://doi.org/10.6084/m9.figshare.25584597 (ref. 59). A larger number of additional neurobehavioural signals used to produce figures and conduct analysis are available from the corresponding authors on reasonable request. Source data for the figures are provided with this paper.

Code availability

Data analysis made use of inbuilt functions in MATLAB and TensorFlow. Custom-developed firmware for BLE SoCs and Android applications (UIs) for use on smartphones made use of inbuilt functions in MCUXpresso IDE and Flutter. All parameters used for analysis are available in Methods and Supplementary Information. All codes for the wireless neural recorder and neurobehavioural signal analysis used in this study are available from the corresponding authors on reasonable request.

References

1. Mayberg, H. S. et al. Deep brain stimulation for treatment-resistant depression. *Neuron* **45**, 651–660 (2005).
2. Boyden, E. S., Zhang, F., Bamberg, E., Nagel, G. & Deisseroth, K. Millisecond-timescale, genetically targeted optical control of neural activity. *Nat. Neurosci.* **8**, 1263–1268 (2005).
3. Jeong, J. W. et al. Wireless optofluidic systems for programmable in vivo pharmacology and optogenetics. *Cell* **162**, 662–674 (2015).
4. Canales, A. et al. Multifunctional fibers for simultaneous optical, electrical and chemical interrogation of neural circuits in vivo. *Nat. Biotechnol.* **33**, 277–284 (2015).
5. Li, J. et al. A tissue-like neurotransmitter sensor for the brain and gut. *Nature* **606**, 94–101 (2022).
6. Buzsáki, G. Large-scale recording of neuronal ensembles. *Nat. Neurosci.* **7**, 446–451 (2004).
7. Jun, J. J. et al. Fully integrated silicon probes for high-density recording of neural activity. *Nature* **551**, 232–236 (2017).

8. Hochberg, L. R. et al. Reach and grasp by people with tetraplegia using a neurally controlled robotic arm. *Nature* **485**, 372–375 (2012).
9. Buzsáki, G. et al. Tools for probing local circuits: high-density silicon probes combined with optogenetics. *Neuron* **86**, 92–105 (2015).
10. Liu, J. et al. Syringe-injectable electronics. *Nat. Nanotechnol.* **10**, 629–636 (2015).
11. Viventi, J. et al. Flexible, foldable, actively multiplexed, high-density electrode array for mapping brain activity in vivo. *Nat. Neurosci.* **14**, 1599–1605 (2011).
12. Yang, X. et al. Bioinspired neuron-like electronics. *Nat. Mater.* **18**, 510–517 (2019).
13. Minev, I. R. et al. Biomaterials. Electronic dura mater for long-term multimodal neural interfaces. *Science* **347**, 159–163 (2015).
14. Kim, C. Y. et al. Soft subdermal implant capable of wireless battery charging and programmable controls for applications in optogenetics. *Nat. Commun.* **12**, 535 (2021).
15. Yang, Y. et al. Wireless multilateral devices for optogenetic studies of individual and social behaviors. *Nat. Neurosci.* **24**, 1035–1045 (2021).
16. Gutruf, P. et al. Fully implantable optoelectronic systems for battery-free, multimodal operation in neuroscience research. *Nat. Electron.* **1**, 652–660 (2018).
17. Montgomery, K. L. et al. Wirelessly powered, fully internal optogenetics for brain, spinal and peripheral circuits in mice. *Nat. Methods* **12**, 969–974 (2015).
18. Shin, G. et al. Flexible near-field wireless optoelectronics as subdermal implants for broad applications in optogenetics. *Neuron* **93**, 509–521.e3 (2017).
19. Herculano-Houzel, S. The human brain in numbers: a linearly scaled-up primate brain. *Front. Hum. Neurosci.* **3**, 31 (2009).
20. Belmonte, J. C. I. et al. Brains, genes, and primates. *Neuron* **86**, 617–631 (2015).
21. Schwarz, D. A. et al. Chronic, wireless recordings of large-scale brain activity in freely moving rhesus monkeys. *Nat. Methods* **11**, 670–676 (2014).
22. Capogrosso, M. et al. A brain–spine interface alleviating gait deficits after spinal cord injury in primates. *Nature* **539**, 284–288 (2016).
23. Borton, D. A., Yin, M., Aceros, J. & Nurmikko, A. An implantable wireless neural interface for recording cortical circuit dynamics in moving primates. *J. Neural Eng.* **10**, 026010 (2013).
24. Weltman, A., Yoo, J. & Meng, E. Flexible, penetrating brain probes enabled by advances in polymer microfabrication. *Micromachines* **7**, 180 (2016).
25. Miller, J. S. et al. Rapid casting of patterned vascular networks for perfusable engineered three-dimensional tissues. *Nat. Mater.* **11**, 768–774 (2012).
26. Takeuchi, S., Ziegler, D., Yoshida, Y., Mabuchi, K. & Suzuki, T. Parylene flexible neural probes integrated with microfluidic channels. *Lab Chip* **5**, 519–523 (2005).
27. Ahn, D. & Hong, S. A study on magnetic field repeater in wireless power transfer. *IEEE Trans. Ind. Electron.* **60**, 360–371 (2013).
28. Cecil, S. et al. Numerical assessment of specific absorption rate in the human body caused by NFC devices. In *2010 Second International Workshop on Near Field Communication* 65–70 (IEEE, 2010).
29. Laffins, M. M., Mellal, N., Almlie, C. L. & Regalia, D. E. Evaluation of infrared thermometry in cynomolgus macaques (*Macaca fascicularis*). *J. Am. Assoc. Lab. Anim. Sci.* **56**, 84–89 (2017).
30. Maruhashi, T. Feeding behavior and diet of the Japanese monkey (*Macaca fuscata yakui*) on Yakushima Island, Japan. *Primates* **21**, 141–160 (1980).
31. Watts, A. G., Kanoski, S. E., Sanchez-Watts, G. & Langhans, W. The physiological control of eating: signals, neurons, and networks. *Physiol. Rev.* **102**, 689–813 (2022).
32. Lee, Y. H. et al. Food craving, seeking, and consumption behaviors: conceptual phases and assessment methods used in animal and human studies. *J. Obes. Metab. Syndr.* **28**, 148–157 (2019).
33. Nieh, E. H. et al. Decoding neural circuits that control compulsive sucrose seeking. *Cell* **160**, 528–541 (2015).
34. Stuber, G. D. & Wise, R. A. Lateral hypothalamic circuits for feeding and reward. *Nat. Neurosci.* **19**, 198–205 (2016).
35. O'Connor, E. C. et al. Accumbal D1R neurons projecting to lateral hypothalamus authorize feeding. *Neuron* **88**, 553–564 (2015).
36. Lee, Y. H. et al. Lateral hypothalamic leptin receptor neurons drive hunger-gated food-seeking and consummatory behaviours in male mice. *Nat. Commun.* **14**, 1486 (2023).
37. Noritake, A. & Nakamura, K. Rewarding-unrewarding prediction signals under a bivalent context in the primate lateral hypothalamus. *Sci. Rep.* **13**, 5926 (2023).
38. Noritake, A. & Nakamura, K. Encoding prediction signals during appetitive and aversive Pavlovian conditioning in the primate lateral hypothalamus. *J. Neurophysiol.* **121**, 396–417 (2019).
39. Burton, M., Rolls, E. & Mora, F. Effects of hunger on the responses of neurons in the lateral hypothalamus to the sight and taste of food. *Exp. Neurol.* **51**, 668–677 (1976).
40. Mansbridge, N. et al. Feature selection and comparison of machine learning algorithms in classification of grazing and rumination behaviour in sheep. *Sensors* **18**, 3532 (2018).
41. Barwick, J., Lamb, D. W., Dobos, R., Welch, M. & Trotter, M. Categorising sheep activity using a tri-axial accelerometer. *Comput. Electron. Agric.* **145**, 289–297 (2018).
42. Kleanthous, N. et al. A survey of machine learning approaches in animal behaviour. *Neurocomputing* **491**, 442–463 (2022).
43. Decandia, M. et al. The effect of different time epoch settings on the classification of sheep behaviour using tri-axial accelerometry. *Comput. Electron. Agric.* **154**, 112–119 (2018).
44. Riaboff, L. et al. Evaluation of pre-processing methods for the prediction of cattle behaviour from accelerometer data. *Comput. Electron. Agric.* **165**, 104961 (2019).
45. Golshan, H. M., Hebb, A. O. & Mahoor, M. H. LFP-Net: a deep learning framework to recognize human behavioral activities using brain STN-LFP signals. *J. Neurosci. Methods* **335**, 108621 (2020).
46. Yamanaka, K. Anodically electrodeposited iridium oxide films (AEIROF) from alkaline solutions for electrochromic display devices. *Jpn. J. Appl. Phys.* **28**, 632 (1989).
47. Park, J. et al. XperCT-guided Intra-cisterna magna injection of streptozotocin for establishing an Alzheimer's disease model using the cynomolgus monkey (*Macaca fascicularis*). *Exp. Neurobiol.* **31**, 409–418 (2022).
48. Jeong, H. S. et al. Brain structural changes in cynomolgus monkeys administered with 1-methyl-4-phenyl-1,2,3,6-tetrahydropyridine: a longitudinal voxel-based morphometry and diffusion tensor imaging study. *PLoS ONE* **13**, e0189804 (2018).
49. Yeo, H. G. et al. Characterization of cerebral damage in a monkey model of Alzheimer's disease induced by intracerebroventricular injection of streptozotocin. *J. Alzheimers Dis.* **46**, 989–1005 (2015).
59. Oh, S. et al. A stealthy neural recorder for the study of behaviour in primates. *figshare* https://doi.org/10.6084/m9.figshare.25584597 (2024).
50. Zhou, A. et al. A wireless and artefact-free 128-channel neuromodulation device for closed-loop stimulation and recording in non-human primates. *Nat. Biomed. Eng.* **3**, 15–26 (2018).
51. Silvernagel, M. P. et al. A markerless platform for ambulatory systems neuroscience. *Sci. Robot.* **6**, eabj7045 (2021).
52. Yoon, Y. et al. Neural probe system for behavioral neuropharmacology by bi-directional wireless drug delivery and electrophysiology in socially interacting mice. *Nat. Commun.* **13**, 5521 (2022).

53. Ouyang, W. et al. A wireless and battery-less implant for multimodal closed-loop neuromodulation in small animals. *Nat. Biomed. Eng.* **7**, 1252–1269 (2023).
54. Mestais, C. S. et al. WIMAGINE: wireless 64-channel ECoG recording implant for long term clinical applications. *IEEE Trans. Neural Syst. Rehabil. Eng.* **23**, 10–21 (2015).
55. Lee, J. et al. Neural recording and stimulation using wireless networks of microimplants. *Nat. Electron.* **4**, 604–614 (2021).
56. Pandarinath, C. et al. High performance communication by people with paralysis using an intracortical brain–computer interface. *eLife* **6**, e18554 (2017).
57. Lorach, H. et al. Walking naturally after spinal cord injury using a brain–spine interface. *Nature* **618**, 126–133 (2023).
58. Steinmetz, N. A. et al. Neuropixels 2.0: a miniaturized high-density probe for stable, long-term brain recordings. *Science* **372**, eabf4588 (2021).

Acknowledgements

This work was supported by the National Research Foundation of Korea (NRF) grant funded by the Korea government (MSIT) (Nos. RS-2024-00460364, RS-2023-00234581).

Author contributions

S.O., J.J., J.W., Y.L. and K.-I.J. designed the project and wrote the manuscript. S.O., J.J., J.W., K.S.L., C.-Y.J., H.-G.Y., Y.G.K., Y.H.L., L.J.H., H.H.J., J.Y., H.L., J.H., J.K., D.L., S.S., J.S., T.S.Y., Jungmin Lee, S.L., Jaehong Lee, B.H.K., J.-W.C., J.-C.R., Y.M.S., J.-W.J., H.J.C., S.X., Y.L. and K.-I.J. carried out experiments and analysed the experimental data. Y.L. and K.-I.J. supervised the project. All authors reviewed and commented on the manuscript.

Competing interests

K.-I.J. is the inventor on a patent application related to this work filed by the ENSIDE Corporation (no. 1025162520000, 2023., no. 1025162510000, 2023., no. 1025254730000, 2023). K.-I.J., S.O. and J.J. have submitted a patent application based on the research described in this manuscript (no. 10-2024-0132404, 2024). K.-I.J. is a founder of ENSIDE Corporation, which offers related technology products.

Additional information

Extended data is available for this paper at https://doi.org/10.1038/s41551-024-01280-w.

Supplementary information The online version contains supplementary material available at https://doi.org/10.1038/s41551-024-01280-w.

Correspondence and requests for materials should be addressed to Youngjeon Lee or Kyung-In Jang.

Peer review information *Nature Biomedical Engineering* thanks Jihun Lee and the other, anonymous, reviewer(s) for their contribution to the peer review of this work. Peer reviewer reports are available.

Reprints and permissions information is available at www.nature.com/reprints.

Publisher's note Springer Nature remains neutral with regard to jurisdictional claims in published maps and institutional affiliations.

[1]Department of Robotics and Mechatronics Engineering, Daegu Gyeongbuk Institute of Science and Technology (DGIST), Daegu, Republic of Korea. [2]Brain Engineering Convergence Research Center, Daegu Gyeongbuk Institute of Science and Technology (DGIST), Daegu, Republic of Korea. [3]National Primate Research Center, Korea Research Institute of Bioscience and Biotechnology (KRIBB), Cheongju, Republic of Korea. [4]Futuristic Animal Resource and Research Center, Korea Research Institute of Bioscience and Biotechnology (KRIBB), Cheongju, Republic of Korea. [5]KRIBB School of Bioscience, Korea National University of Science and Technology (UST), Daejeon, Republic of Korea. [6]Department of Biomedical Sciences, Seoul National University College of Medicine, Seoul, Republic of Korea. [7]Wide River Institute of Immunology, Seoul National University College of Medicine, Seoul, Republic of Korea. [8]Department of Electrical Engineering and Computer Science, Daegu Gyeongbuk Institute of Science and Technology (DGIST), Daegu, Republic of Korea. [9]Hertie Institute for Clinical Brain Research, International Max Planck Research School and University of Tuebingen, Tuebingen, Germany. [10]Department of Brain Sciences, Daegu Gyeongbuk Institute of Science and Technology (DGIST), Daegu, Republic of Korea. [11]Korea Brain Research Institute (KBRI), Daegu, Republic of Korea. [12]School of Electrical Engineering and Computer Science, Gwangju Institute of Science and Technology (GIST), Gwangju, Republic of Korea. [13]School of Electrical Engineering, Korea Advanced Institute of Science and Technology (KAIST), Daejeon, Republic of Korea. [14]Department of Nanoengineering, University of California San Diego, La Jolla, CA, USA. [15]Artificial Intelligence Major in Department of Interdisciplinary Studies, Daegu Gyeongbuk Institute of Science and Technology (DGIST), Daegu, Republic of Korea. [16]Institute of Next-generation Semiconductor Convergence Technology, Daegu Gyeongbuk Institute of Science and Technology (DGIST), Daegu, Republic of Korea. [17]Sensorium Institute, Daegu Gyeongbuk Institute of Science and Technology (DGIST), Daegu, Republic of Korea. [18]ENSIDE Corporation, Daegu, Republic of Korea. [19]These authors contributed equally: Saehyuck Oh, Janghwan Jekal, Jinyoung Won. ✉e-mail: neurosci@kribb.re.kr; kijang@dgist.ac.kr

https://doi.org/10.1038/s41551-024-01280-w

a. Comparative analysis of our neural recorder and previously reported recorders.

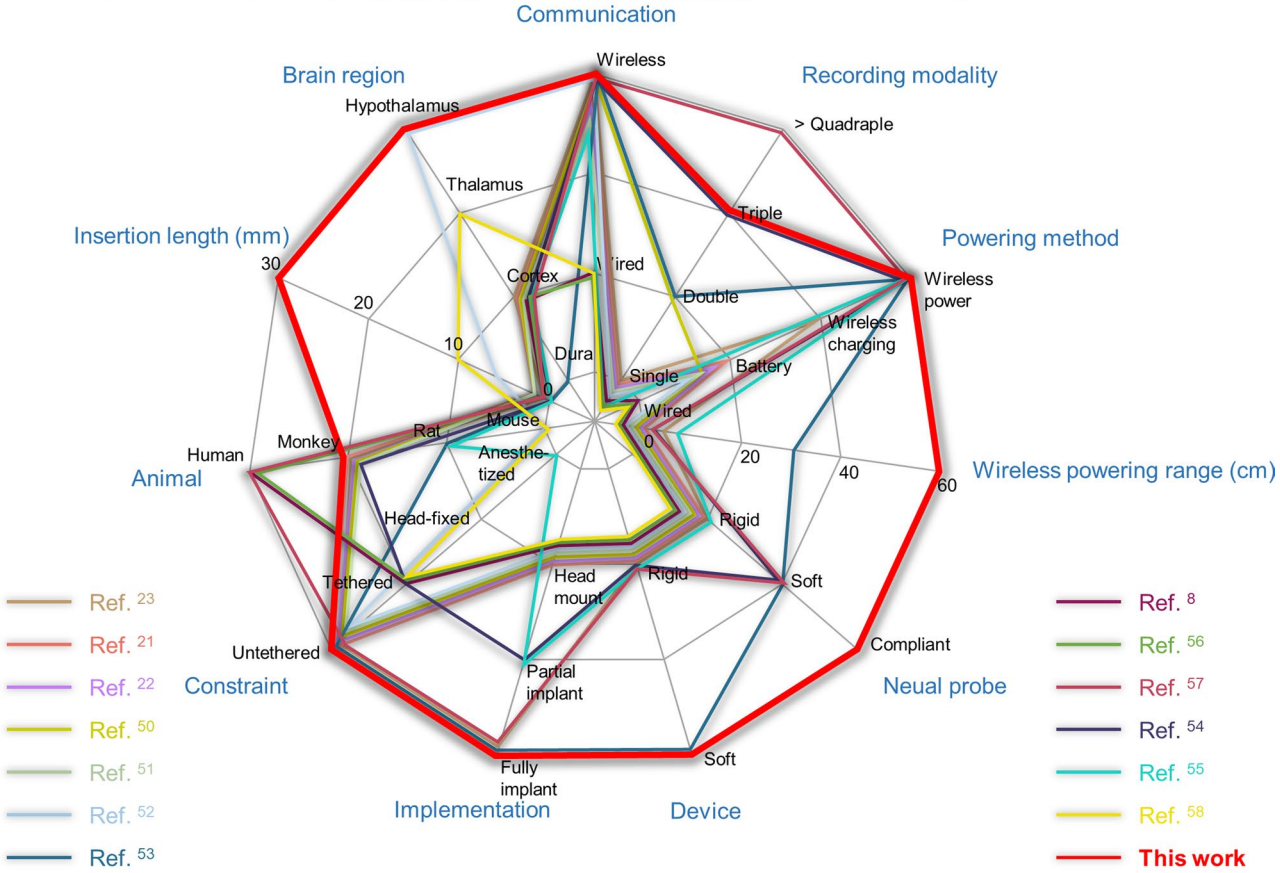

b. Stealthy neural recording during natural instinctive behavior in the monkey.

Extended Data Fig. 1 | See next page for caption.

https://doi.org/10.1038/s41551-024-01280-w

Extended Data Fig. 1 | Comparative features and application of the stealthy neural recorder. a, A spider web graphical representation of categorized specifications for recently reported highly integrated neural recorders and this work[50,51,52,53,54–56,57,58]. Despite the advancements in neural recording devices thus far, a neural recorder integrating all essential device functions for studying neural activity on naturalistic behaviour have not been developed until this work. **b**, Photograph of wireless neurobehavioural signal monitoring of the freely moving monkey in real time while the monkey ate a banana in a forest-like environment.

https://doi.org/10.1038/s41551-024-01280-w

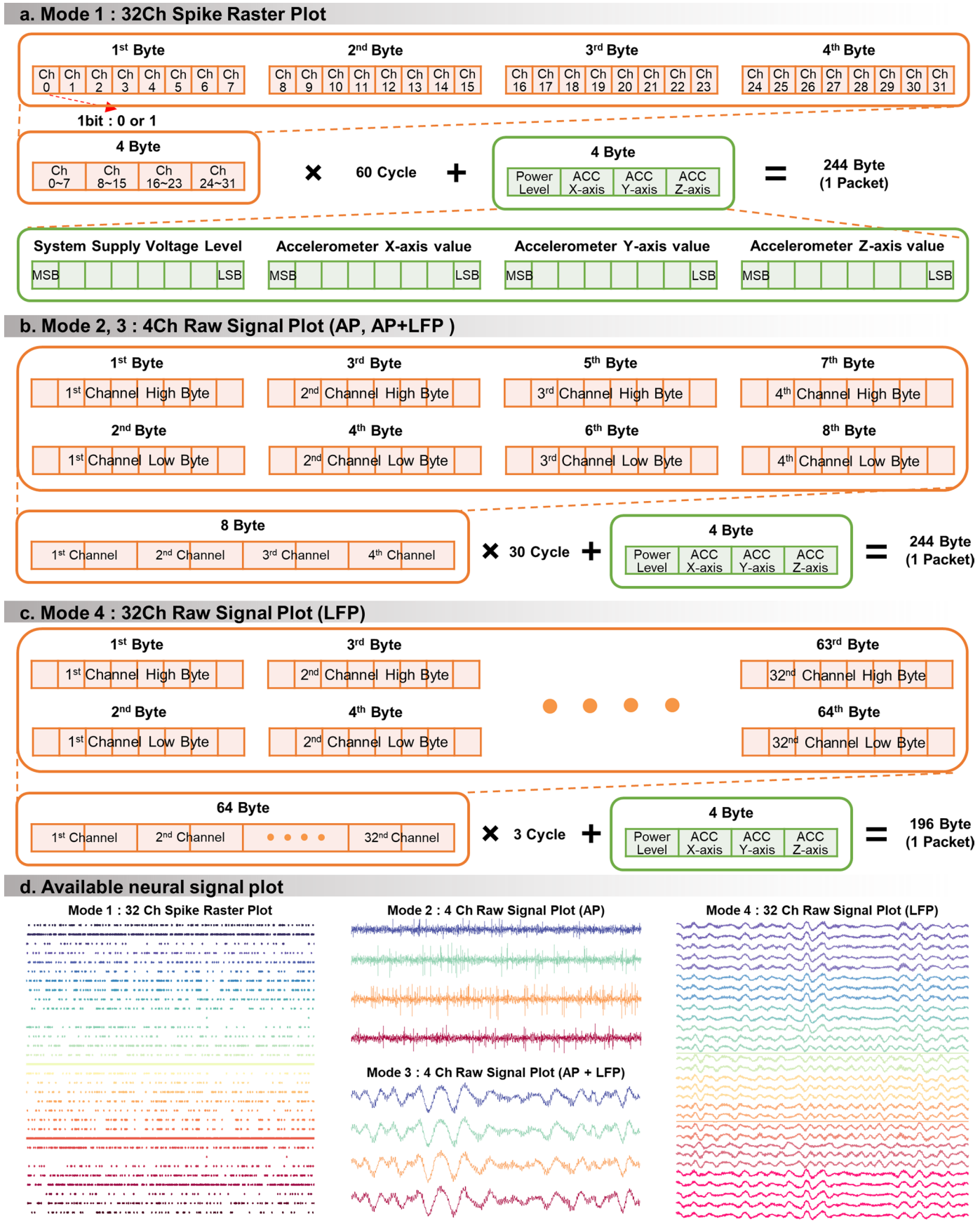

Extended Data Fig. 2 | See next page for caption.

https://doi.org/10.1038/s41551-024-01280-w

Extended Data Fig. 2 | Firmware mode, data-packet structure and available neural signal plots. a, Data packet structure of 32-channel spike raster plot to show the firing patterns of individual neurons in 32 channels. **b**, Data packet structure of the 4-channel raw signal plot to capture neural signals at a high sampling rate (11 kSa/s) on 4 channels to classify the shape of neural spikes. **c**, Data packet structure of a 32-channel raw signal plot to show LFPs to gain insight into the collective electrophysiological activity of neurons in a particular brain region. **d**, Representative measured neural signals by the stealthy neural recorder using a neural simulator (FB128, TDT) depending on available firmware modes. The stealthy neural recorder provides four distinct modes to measure brain neural signals, allowing for the tailoring of the frequency band and the number of channels to focus on specific neurophysiological information. Each firmware mode has a different frequency band (Mode 1 and 2: 300-5000 Hz; Mode 3: 0.5-5000 Hz; Mode 4: 0.5-300 Hz), sampling frequency (Mode 1, 2 and 3: 11 kSa/s, Mode 4: 0.9 kSa/s) and data rate (Mode 1: 46 kB/s; Mode 2 and 3: 92 kB/s; Mode 4: 60 kB/s).

https://doi.org/10.1038/s41551-024-01280-w

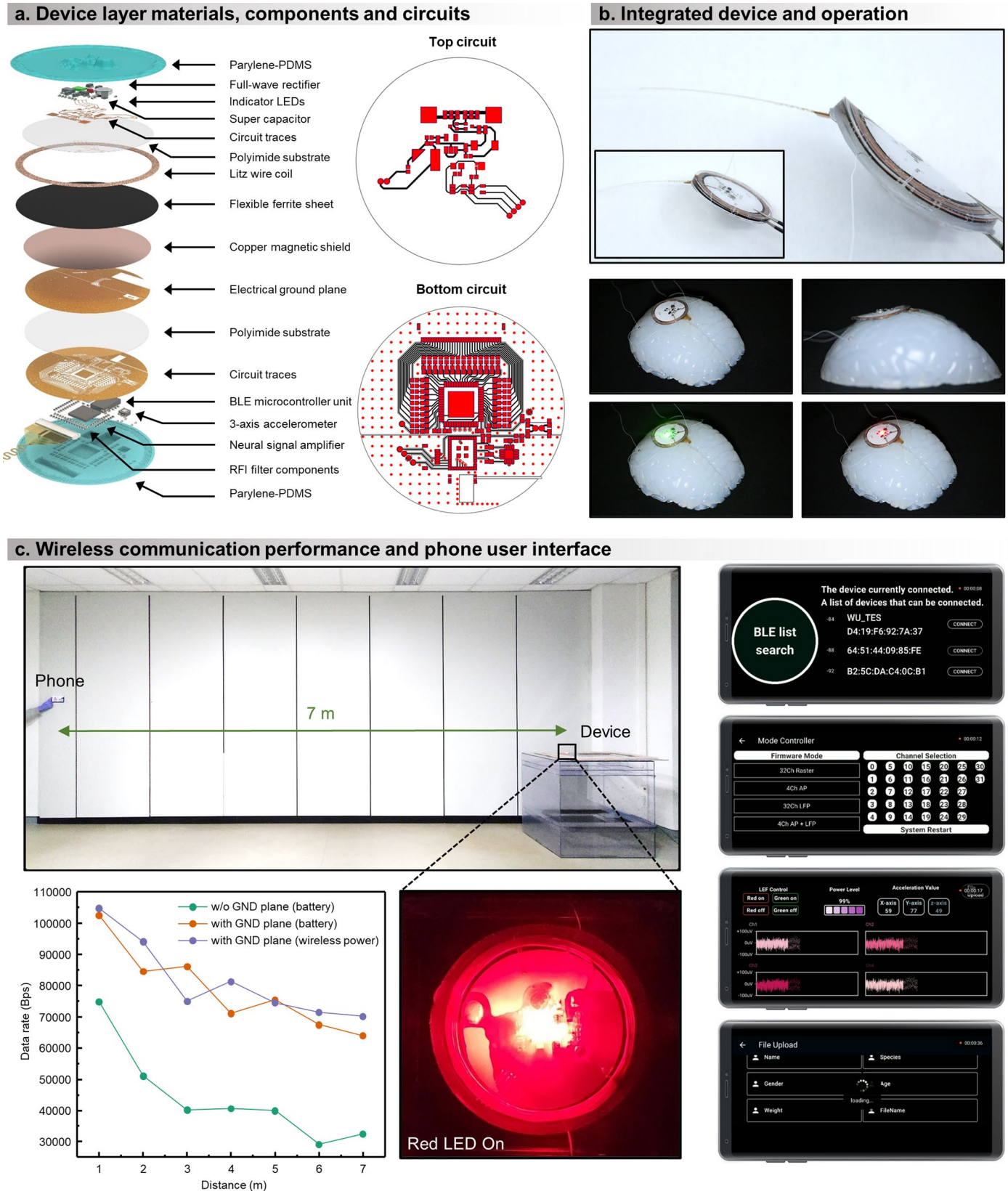

Extended Data Fig. 3 | Device structure, operation and wireless communication with the user interface. a, Schematic illustration of layer materials, electrical components and circuits of the stealthy neural recorder. **b**, Optical images of the integrated stealthy neural recorder and wireless LED operation controlled by a customized phone user interface. **c**, Photographs of the experimental setup to verify wireless communication performance with the smartphone user interface and wireless data rate over a distance.

https://doi.org/10.1038/s41551-024-01280-w

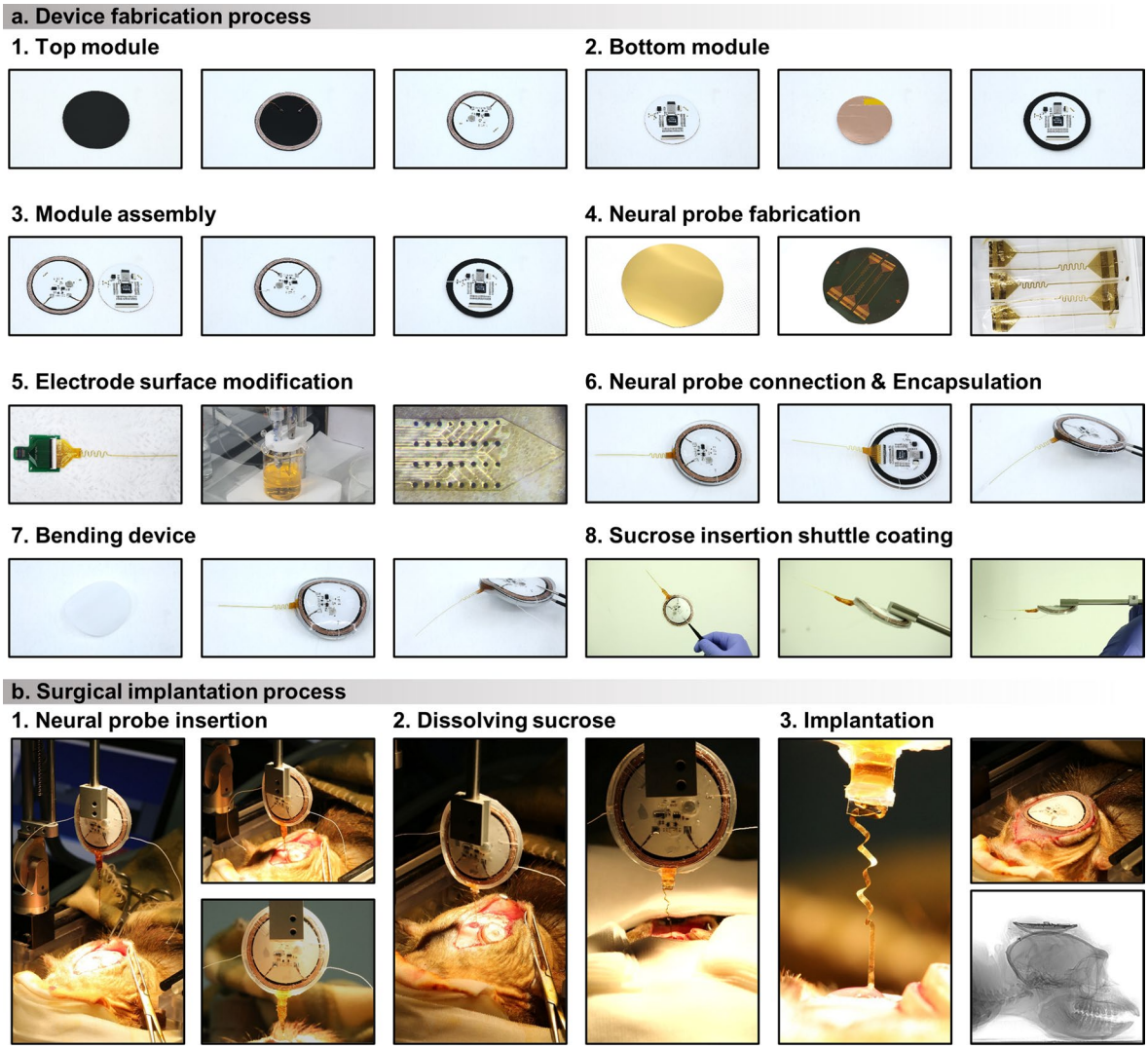

Extended Data Fig. 4 | Device fabrication and surgical implantation process. a, Photographs showing the entire fabrication process of the stealthy neural recorder. **b**, Surgical implantation process to insert a neural probe into the monkey brain and implant the stealthy neural recorder under the scalp.

https://doi.org/10.1038/s41551-024-01280-w

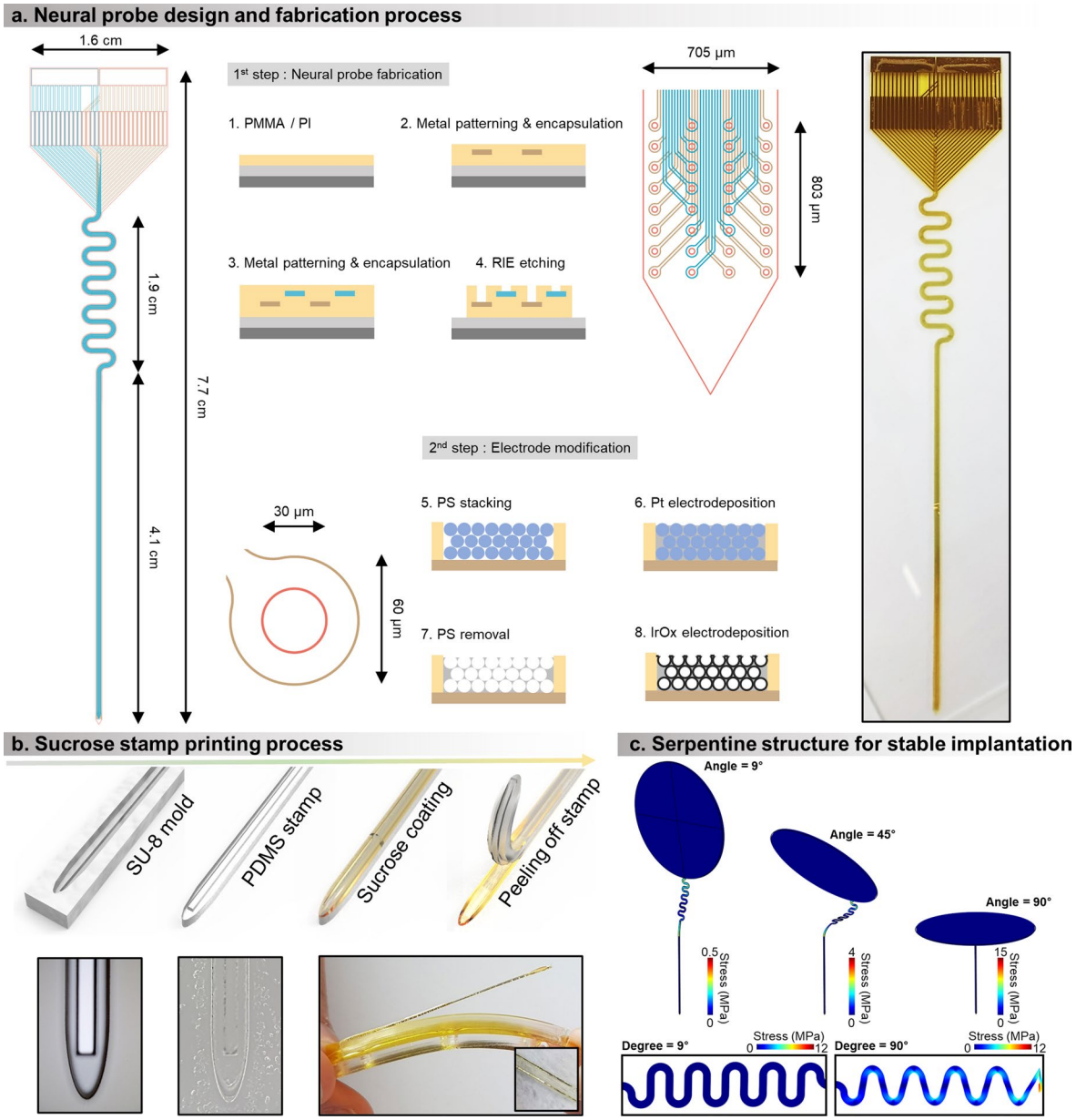

Extended Data Fig. 5 | Neural probe, sucrose insertion shuttle design, and fabrication process. a, CAD design, optical image of the neural probe, and schematic illustration of the fabrication process of the neural probe with nanoporous electrodes. **b**, Schematic illustration (top) and optical images (bottom) of the stamp printing process of the U-beam sucrose insertion shuttle. **c**, FEA simulations of the serpentine interconnect of the neural probe according to the rotation angle of the device for stable implantation.

https://doi.org/10.1038/s41551-024-01280-w

a. Surgical environment and flow for non-human primates

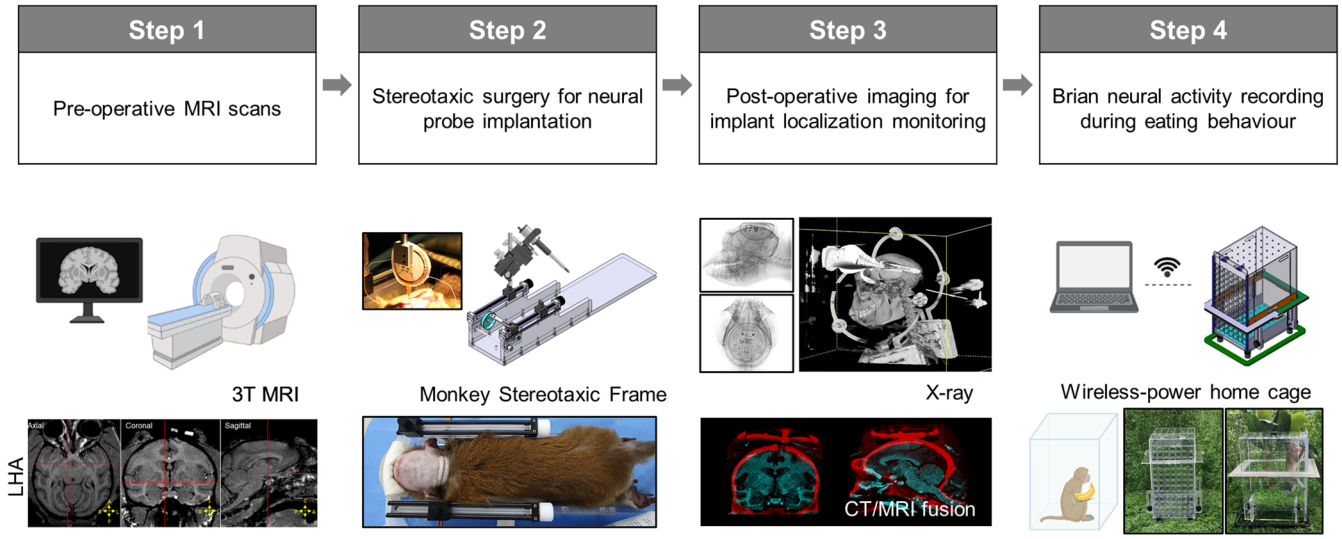

b. Histological results (rodents)

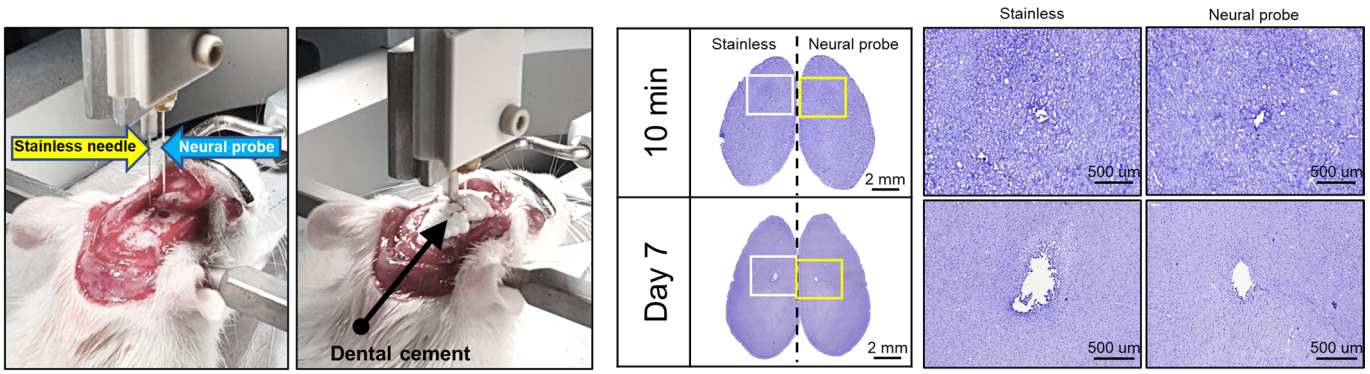

c. Histological results (primates)

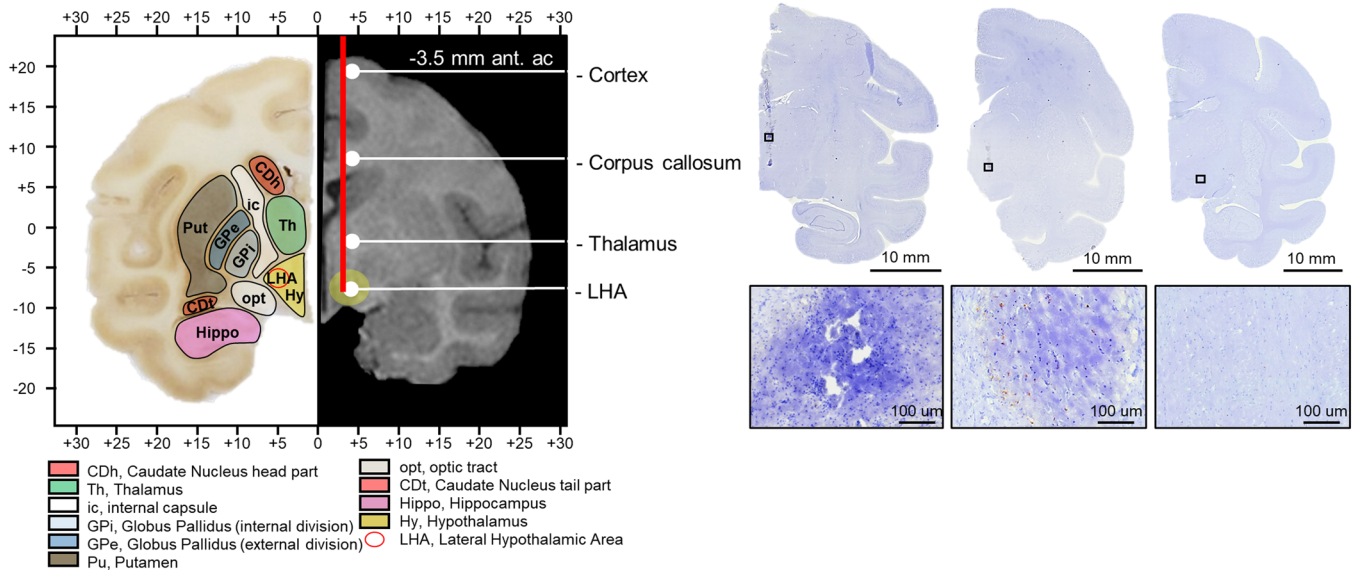

Extended Data Fig. 6 | See next page for caption.

https://doi.org/10.1038/s41551-024-01280-w

Extended Data Fig. 6 | Diagram of the experimental setup, and histological analysis of the rat and monkey brain. a, Experimental setup for neural probe implantation and neurobehavioural signal monitoring. Step 1: Pre-operative MRI scanning was performed, providing anatomical information as a baseline reference for targeting the LHA brain region. Step 2: The neural probe was inserted into the monkey brain using a custom-built stereotaxic frame for brain neural signal recording. Step 3: After stereotaxic surgery, post-operative CT and MRI were performed to confirm the location of the neural probe. Step 4: Brain neural activity was recorded during eating behaviour in a wireless-power home cage. **b**, Histological analysis of the rat brain tissue around the neural probe and stainless needle. Photographs of the neural probe and stainless needle insertion into the cerebral cortex (left). Stainless steel needles with a diameter of 300 μm were used as a negative control. Dental cement was used for implantation. Representative brain sections after undergoing cresyl violet acetate (Nissl) staining at 10 min and Day 7 post-implantation (right). **c**, Histological analysis of the monkey brain tissue around the neural probe. A coronal section (3.5 mm posterior to the anterior commissure) from a representative macaque monkey brain showing the neural probe track (red line) passing through the cortex, corpus callosum and thalamus and targeting the LHA (yellow area) (left). Representative brain sections for Nissl staining at 2 weeks, 4 weeks, and 12 weeks post-implantation (right). The schematics in a were created by BioRender.

https://doi.org/10.1038/s41551-024-01280-w

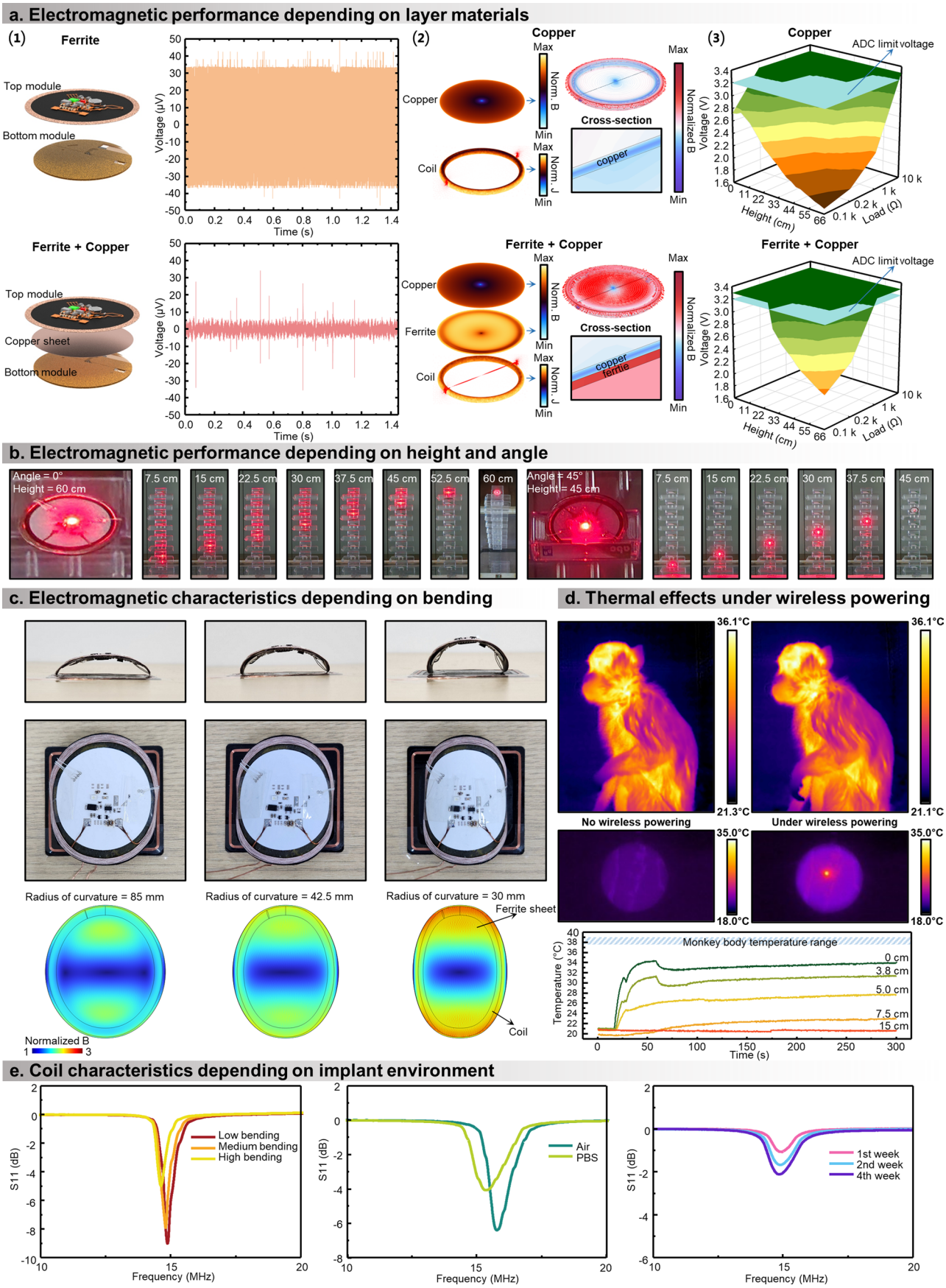

Extended Data Fig. 7 | See next page for caption.

https://doi.org/10.1038/s41551-024-01280-w

Extended Data Fig. 7 | Effects of the material, design and implant environment on wireless power transfer. a, Differences in noise sensitivity with or without a copper sheet. The in vitro test using a neural simulator (FB128, TDT) shows that RF noise from the incoming magnetic field completely buries neural spikes in the stealthy neural recorder without the copper sheet, whereas neural spikes are well measured in the device with the copper sheet (1). FEA simulations of differences in magnetic flux density and current density of the wireless power receiver with (bottom) or without (top) the ferrite sheet. The ferrite sheet shows a high magnetic flux density, even if there is a metallic object nearby, allowing a large current to be induced in the coil (2). The regulated output voltage according to the distance from the repeater coil with variable loads. The graph shows differences in the wireless power transfer range for battery-free operation of the stealthy neural recorder with (bottom) or without (top) the ferrite sheet (3). **b**, Photographs showing red LED operation according to distance from the repeater coil and device rotation angle. **c**, Measurement setup of the RF behaviour (top, middle) of the stealthy neural recorder and FEA simulations (bottom) of the magnetic flux density focused on the ferrite sheet according to bending curvatures of the device. **d**, IR images of the monkey (top) and device (middle) under wireless power. Maximum temperature of the stealthy neural recorder according to the distance from the repeater coil and wireless power transfer time (bottom). The device was placed in an open-air environment, specifically positioned at an equal height adjacent to the corner of a repeater coil that produces a strong magnetic field. **e**, RF behaviour of the stealthy neural recorder according to bending (left) and the surrounding medium (middle). RF behaviour of the implanted stealthy neural recorder in vivo during one month of implantation (right).

https://doi.org/10.1038/s41551-024-01280-w

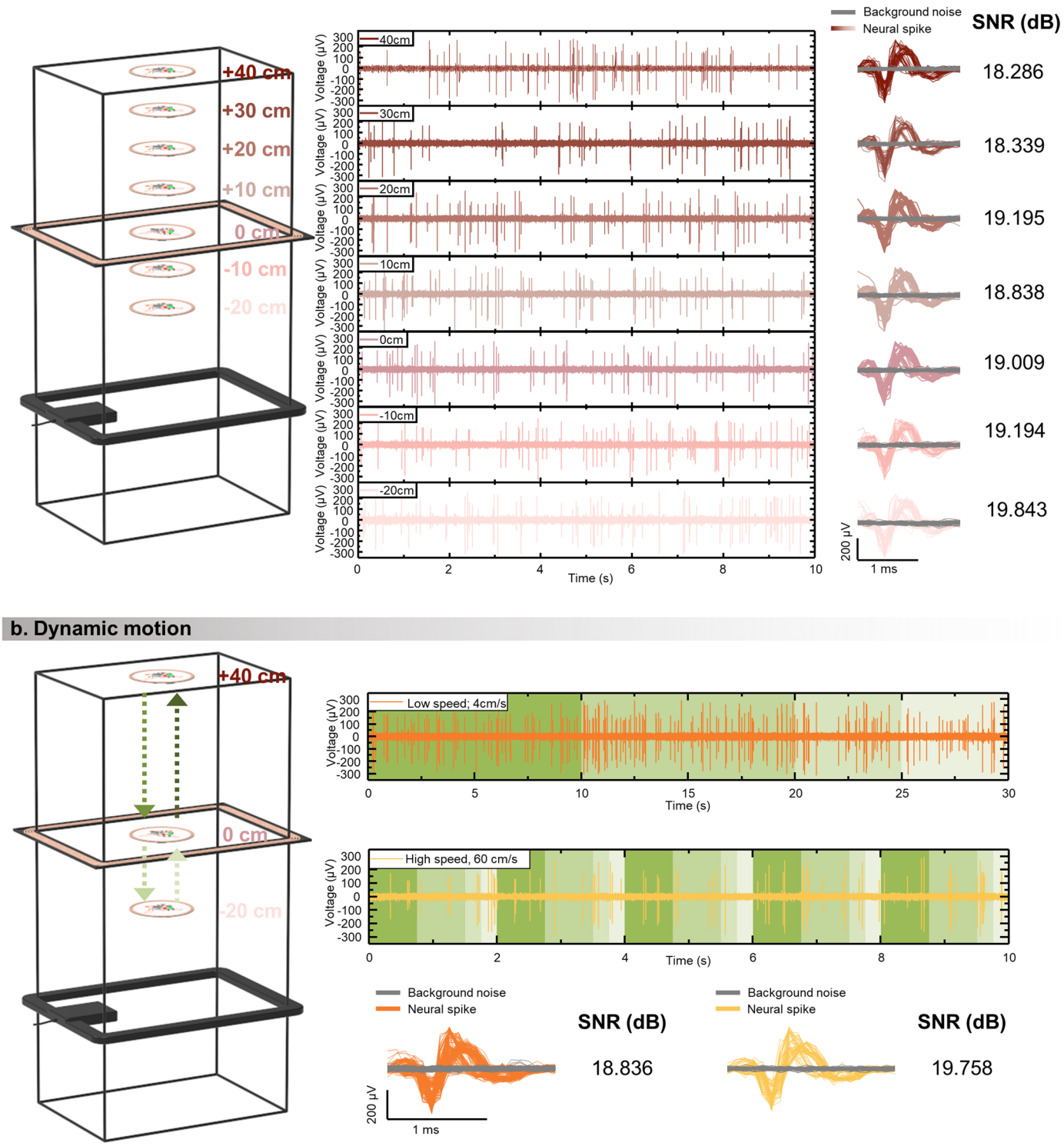

Extended Data Fig. 8 | Noise immunity under wireless power transmission. a, **b**, Experimental results to determine the noise characteristics of the wirelessly powered stealthy neural recorder using a neural simulator (FB128, TDT) in preparation for situations where the freely moving monkey is still (**a**) or in motion (**b**).

https://doi.org/10.1038/s41551-024-01280-w

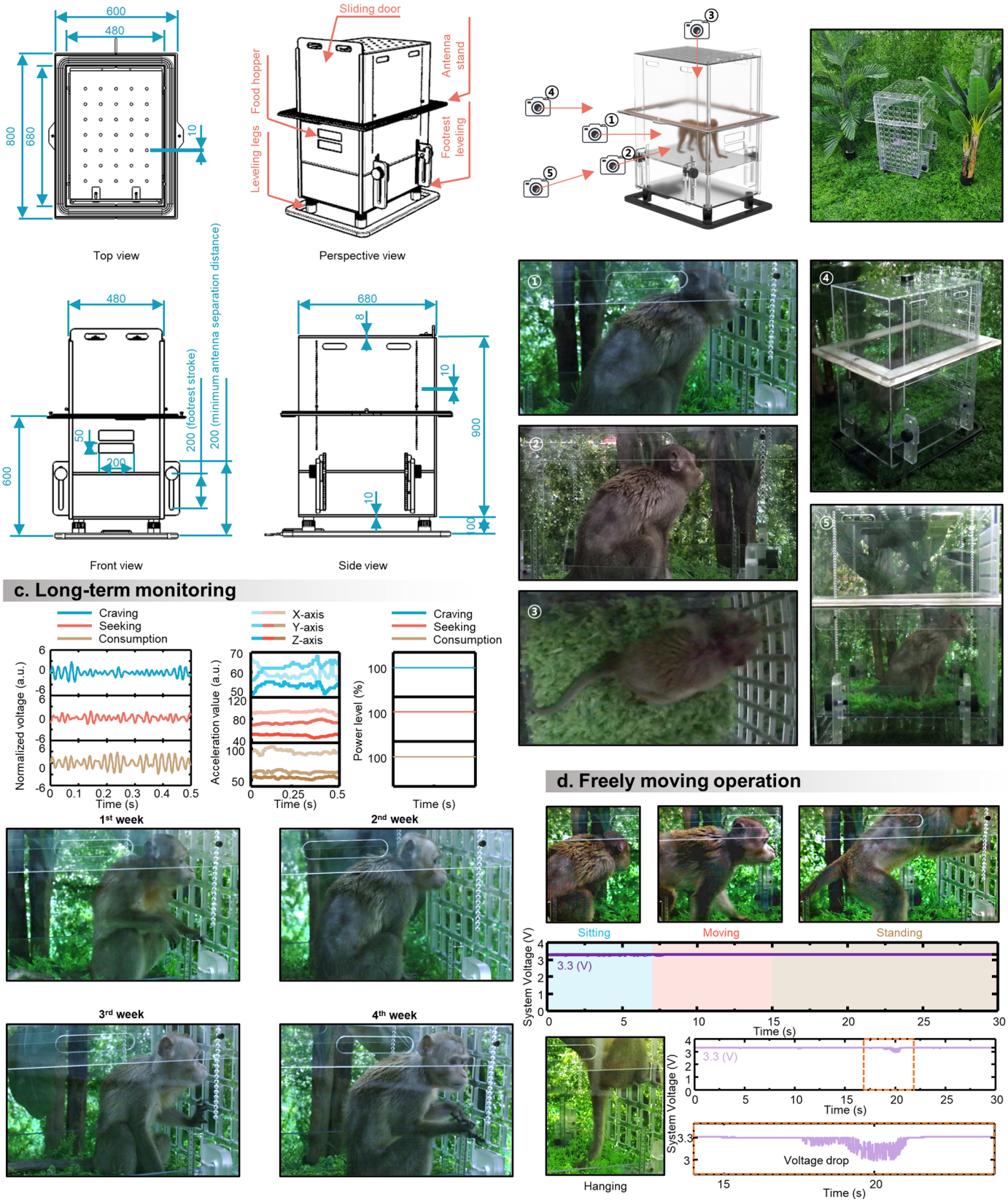

Extended Data Fig. 9 | Neurobehavioural monitoring of NHPs in a forest-like environment. a, Customized design of an acrylic wireless-power home cage for NHPs. **b**, Forest-like environment for naturalistic behaviours of NHPs and video camera position for monitoring and analysing monkey behaviours. **c**, Representative neurobehavioural signals of the monkey and system power level after one month of implantation (top) and photographs (middle, bottom) of the monkey over that month in the cage. **d**, Voltage profile of the implanted device when the monkey sat, moved, stood and hung in the wireless-power home cage.

https://doi.org/10.1038/s41551-024-01280-w

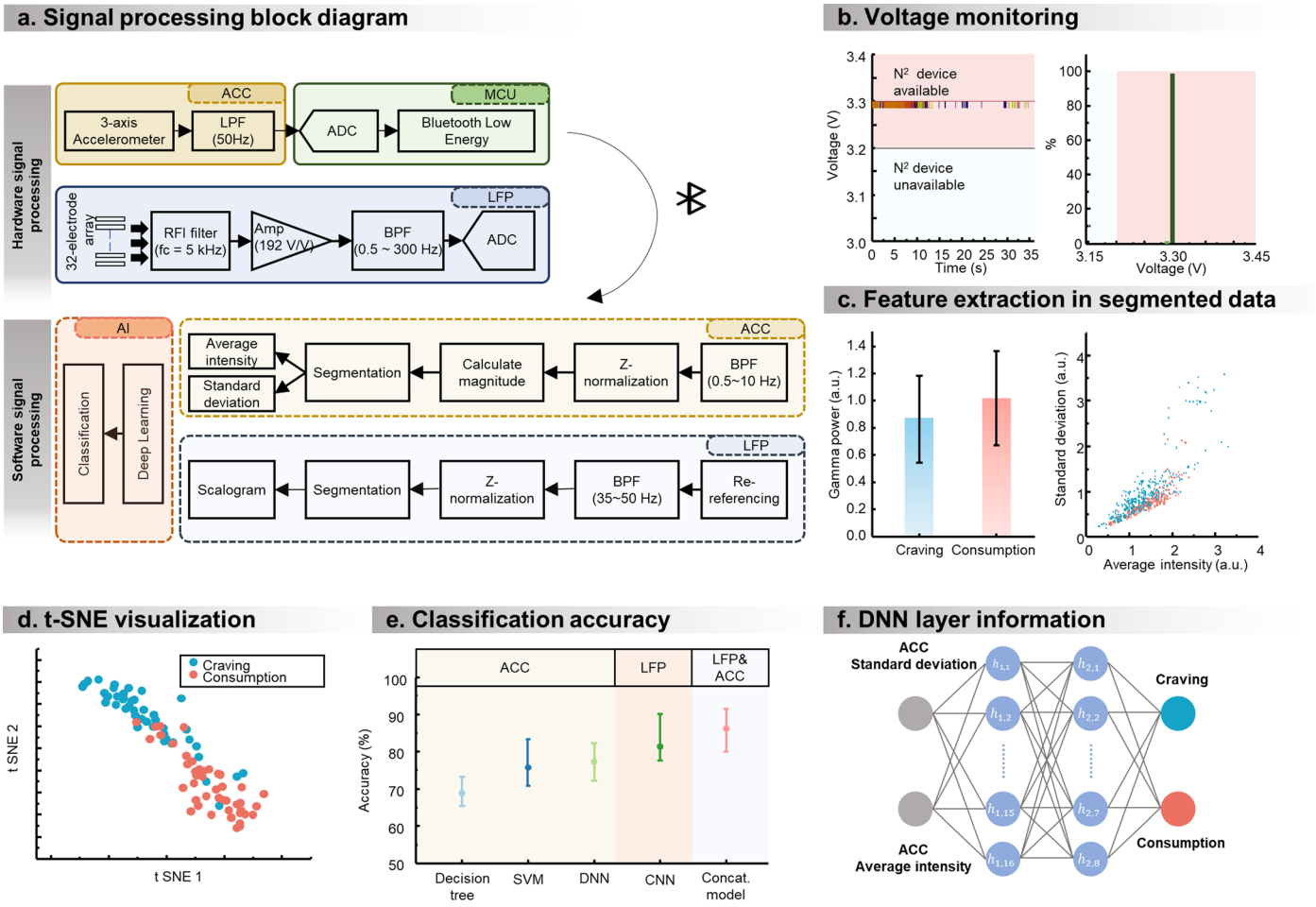

Extended Data Fig. 10 | See next page for caption.

https://doi.org/10.1038/s41551-024-01280-w

Extended Data Fig. 10 | Signal processing and analysis details. a, Block diagram of neurobehavioural signal recording and analysis. **b**, Received power as monitored during eating behaviour experiments. **c**, Averaged gamma power (35-50 Hz) of segmented LFPs in the craving (blue) and consumption (red) phases during eating behaviour experiments. (n = 315 segments, left). Feature extraction results of segmented acceleration data in the consumption phase (red) and the craving phase (blue) (n = 315 segments, right). Error bars represent the standard deviation of the data. **d**, T-distributed stochastic neighbor embedding (t-SNE) visualization of feature output from the concatenated model using recorded neurobehavioural signal. **e**, Comparison of the classification accuracy of 5 classifier models over five folds, utilizing a 4 s time window and 75% overlap for segmentation. **f**, DNN model architecture with extracted acceleration features. **g**, CNN model architecture with extracted scalograms from LFPs. **h**, Detailed structure of the proposed concatenated model consisting of the DNN and CNN.

nature portfolio

Corresponding author(s): Youngjeon Lee and Kyung-In Jang

Last updated by author(s): Apr 11, 2024

Reporting Summary

Nature Portfolio wishes to improve the reproducibility of the work that we publish. This form provides structure for consistency and transparency in reporting. For further information on Nature Portfolio policies, see our Editorial Policies and the Editorial Policy Checklist.

Statistics

For all statistical analyses, confirm that the following items are present in the figure legend, table legend, main text, or Methods section.

n/a	Confirmed
☐	☒ The exact sample size (*n*) for each experimental group/condition, given as a discrete number and unit of measurement
☐	☒ A statement on whether measurements were taken from distinct samples or whether the same sample was measured repeatedly
☐	☒ The statistical test(s) used AND whether they are one- or two-sided *Only common tests should be described solely by name; describe more complex techniques in the Methods section.*
☒	☐ A description of all covariates tested
☐	☒ A description of any assumptions or corrections, such as tests of normality and adjustment for multiple comparisons
☐	☒ A full description of the statistical parameters including central tendency (e.g. means) or other basic estimates (e.g. regression coefficient) AND variation (e.g. standard deviation) or associated estimates of uncertainty (e.g. confidence intervals)
☐	☒ For null hypothesis testing, the test statistic (e.g. *F*, *t*, *r*) with confidence intervals, effect sizes, degrees of freedom and *P* value noted *Give P values as exact values whenever suitable.*
☒	☐ For Bayesian analysis, information on the choice of priors and Markov chain Monte Carlo settings
☒	☐ For hierarchical and complex designs, identification of the appropriate level for tests and full reporting of outcomes
☒	☐ Estimates of effect sizes (e.g. Cohen's *d*, Pearson's *r*), indicating how they were calculated

Our web collection on statistics for biologists contains articles on many of the points above.

Software and code

Policy information about availability of computer code

Data collection	Custom Android application that runs on a smartphone (LG V30). Custom Matlab codes that run on a laptop (ASUS ZenBook 14). Custom-developed firmware for BLE MCUs (MCUXpresso v11.9.0), Android applications (user interfaces) for use on smartphones (Flutter), Matlab codes for use on laptops (Matlab 2021b, 2022b) are available from the corresponding author on reasonable request. COMSOL (Multiphysics 6.1) was used for electromagnetic simulation.
Data analysis	COMSOL (Multiphysics 6.1) Matlab 2021b, 2022b (Mathworks) Microsoft Office 365 Excel Origin Pro 2023 (Origin Lab) FLIR Research IR software 4 (Research IR Max, FLIR systems) TensorFlow (Google)

For manuscripts utilizing custom algorithms or software that are central to the research but not yet described in published literature, software must be made available to editors and reviewers. We strongly encourage code deposition in a community repository (e.g. GitHub). See the Nature Portfolio guidelines for submitting code & software for further information.

Data

Policy information about availability of data

All manuscripts must include a data availability statement. This statement should provide the following information, where applicable:

- Accession codes, unique identifiers, or web links for publicly available datasets
- A description of any restrictions on data availability
- For clinical datasets or third party data, please ensure that the statement adheres to our policy

The main data supporting the results in this study are available within the paper and its Supplementary Information, and also from figshare with the identifier https://doi.org/10.6084/m9.figshare.25584597. Source data for the figures are provided with this paper. A larger number of additional neurobehavioural signals used to produce figures and conduct analysis are available from the corresponding authors on reasonable request.

Research involving human participants, their data, or biological material

Policy information about studies with human participants or human data. See also policy information about sex, gender (identity/presentation), and sexual orientation and race, ethnicity and racism.

Reporting on sex and gender	The study did not involve human research participants.
Reporting on race, ethnicity, or other socially relevant groupings	–
Population characteristics	–
Recruitment	–
Ethics oversight	–

Note that full information on the approval of the study protocol must also be provided in the manuscript.

Field-specific reporting

Please select the one below that is the best fit for your research. If you are not sure, read the appropriate sections before making your selection.

☒ Life sciences ☐ Behavioural & social sciences ☐ Ecological, evolutionary & environmental sciences

For a reference copy of the document with all sections, see nature.com/documents/nr-reporting-summary-flat.pdf

Life sciences study design

All studies must disclose on these points even when the disclosure is negative.

Sample size	One device was implanted in a monkey for the in vivo studies on neurobehavioural signal recording and analysis (shown in Fig. 5). No sample-size calculations were performed, because the goal of this study was to report neural interface technology.
Data exclusions	Data from failed devices were excluded from analysis.
Replication	Neurobehavioural signals (acceleration and neural signals) were recorded in a monkey during eating behaviours for one month. The devices performed similarly across several experiments.
Randomization	The monkey model was chosen for the proof-of-concept experiments. All tested devices were randomly selected.
Blinding	The investigators were blinded to group allocation during data collection and analysis.

Reporting for specific materials, systems and methods

We require information from authors about some types of materials, experimental systems and methods used in many studies. Here, indicate whether each material, system or method listed is relevant to your study. If you are not sure if a list item applies to your research, read the appropriate section before selecting a response.

Materials & experimental systems

n/a	Involved in the study
☒	☐ Antibodies
☒	☐ Eukaryotic cell lines
☒	☐ Palaeontology and archaeology
☐	☒ Animals and other organisms
☒	☐ Clinical data
☒	☐ Dual use research of concern
☒	☐ Plants

Methods

n/a	Involved in the study
☒	☐ ChIP-seq
☒	☐ Flow cytometry
☐	☒ MRI-based neuroimaging

Animals and other research organisms

Policy information about studies involving animals; ARRIVE guidelines recommended for reporting animal research, and Sex and Gender in Research

Laboratory animals	Cynomolgus monkeys (Macaca fascicularis) were obtained from Suzhou Xishan Zhongke Laboratory Animal Co. (Suzhou, China) and housed in individual indoor cages at the National Primate Research Center (NPRC) of the Korea Research Institute of Bioscience and Biotechnology (KRIBB). Sprague–Dawley rats (8-weeks old; 250–280 g) were used for histology.
Wild animals	The study did not involve wild animals.
Reporting on sex	No sex-based analyses were performed, because the device is agnostic to signal inputs and both sexes have comparable physiological responses.
Field-collected samples	The study did not involve samples collected from the field.
Ethics oversight	All experimental procedures involving animal care and the use of NHPs were approved by the Korea Research Institute of Bioscience and Biotechnology (KRIBB) Institutional Animal Care and Use Committee (KRIBB-AEC-21102). All experimental procedures on rats were approved by the Animal Care and Use Committee of the Daegu Gyeongbuk Institute of Science & Technology (DGIST, IACUC 21081101-0002).

Note that full information on the approval of the study protocol must also be provided in the manuscript.

Magnetic resonance imaging

Experimental design

Design type	Stereotactic implantation of a neural probe.
Design specifications	T1-weighted 3D Turbo Field Echo sequence (T1W 3D TFE) with a 32-channel head coil. The total acquisition time was about 13 min 13 s per monkey.
Behavioral performance measures	The study did not involve measurements of human behavioral performance.

Acquisition

Imaging type(s)	Structural MRI
Field strength	3.0 Tesla
Sequence & imaging parameters	Three-dimensional (3D) coronal T1-weighted images were acquired using Turbo Field Echo sequence, with TR/TE = 14/6.9 ms, 150×150 field-of-view (FOV), matrix size 300×300, 1.0 mm slice thickness, –0.5mm slice gap, flip angle 8°, acquisition voxel size 0.5×0.5×0.5 and number of slices 200, average 4.
Area of acquisition	A whole-brain scan.

Diffusion MRI ☐ Used ☒ Not used

Preprocessing

Preprocessing software	Brainsight software vet v2.4
Normalization	Each monkey was its own control
Normalization template	Each monkey was its own control

Noise and artifact removal: No noise or artifact removal

Volume censoring: No volume censoring

Statistical modeling & inference

Model type and settings: The study did not involve statistical modeling and inference.

Effect(s) tested: The study did not involve statistical modeling and inference.

Specify type of analysis: ☐ Whole brain ☒ ROI-based ☐ Both

Anatomical location(s): Region of interest (ROI) was defined manually around lateral hypothalamic area (LHA) by assessing the Paxinos Macaque Brain Atlas.

Statistic type for inference (See Eklund et al. 2016): The study did not involve statistical modeling and inference.

Correction: The study did not involve statistical modeling and inference.

Models & analysis

n/a	Involved in the study
☒	☐ Functional and/or effective connectivity
☒	☐ Graph analysis
☒	☐ Multivariate modeling or predictive analysis